Evolving Earth 3 (2025) 100073

Contents lists available at ScienceDirect

Evolving Earth

journal homepage: www.sciencedirect.com/journal/evolving-earth

Anaerobic photoferrotrophy and hydrothermal influence in the Mesoarchean Girar banded iron formation: insights from micropaleontology and geochemistry

Arif H. Ansari [a,b,*], Yogmaya Shukla [a,b], Gaurav K. Singh [c], Archana Sonker [a,b], Mohammad Arif Ansari [a,b], Arunaditya Das [a,b]

[a] Birbal Sahni Institute of Palaeosciences, Lucknow, Uttar Pradesh, India
[b] Academy of Scientific and Innovative Research, Ghaziabad, Uttar Pradesh, India
[c] Dr. Hari Singh Gour Vishwavidyalaya, Sagar, Madhya Pradesh, India

ARTICLE INFO

Keywords:
Bundelkhand craton
Mesoarchean
Girar
Banded iron formation
Huroniospora
photoferrotrophs

ABSTRACT

Banded Iron Formations (BIFs) serve as critical archives of early biosignatures; however, uncertainties remain regarding the biological affinities, metabolic pathways, and their role in Earth's early oxidation history. This study investigates the Mesoarchean Girar BIF (2850 ± 26 Ma) from the Bundelkhand craton using an integrated micropaleontological and geochemical approach to address these questions. Well-preserved spheroidal microfossils, morphologically similar to *Huroniospora*, are documented. The organic carbon isotopic signatures (δ^{13}C-org ranging from −27.8 ‰ to −35.2 ‰) indicate a biological origin mainly linked to anoxygenic photosynthesizers, methanogenic archaea, or methanotrophic bacteria, and to some extent cyanobacterial activity. These observations suggest that Fe^{2+} oxidation within the Girar-Baraitha BIF was predominantly driven by anaerobic photoferrotrophs, rather than abiotic processes. Geochemical proxies, including Sm/Yb versus Eu/Sm ratios, point to hydrothermal fluid and seawater mixing in proportions of 1:1000 to 1:100, supported by a pronounced positive Eu/Eu* (>2), indicating substantial hydrothermal Fe input. Collectively, these findings provide evidence that anaerobic photosynthesis, particularly photoferrotrophy, played a central role in iron deposition in the Girar-Baraitha BIF. Abiotic oxidation, while present, was likely a secondary process facilitated by localized oxidative conditions. This study contributes to a more nuanced understanding of early Earth's biogeochemical cycles, microbial ecosystems, and the mechanisms driving surface oxidation and iron formation during the Mesoarchean.

1. Introduction

Early Earth's hydrosphere was predominantly anoxic and its chemistry was relatively more influenced by the pulsed release of hydrothermal fluids from deep-sea hydrothermal vents (Derry and Jacobsen, 1990; Jacobsen and Pimentel-Klose, 1988; Kappler and Straub, 2005; Konhauser et al., 2017; Morris, 1993; Morris and Horwitz, 1983; Mukhopadhyay, 2020; Simonson et al., 2003; Wang et al., 2024a, 2024b). Deep-sea hydrothermal vents also released massive amounts of reduced iron ions, i.e., Fe^{2+}, which in the sea surface waters oxidized to water-insoluble Fe^{3+} to form bands of iron-rich sedimentary deposits often alternating with silica-rich bands, known as banded iron formation (BIF). This phenomenon of BIF deposition occurred on a massive scale during 4.3–1.8 Ga (Klein, 2005; Mukhopadhyay, 2020; O'Neil, 2023). Among the commonly accepted pathways for Fe^{2+} oxidation leading to BIF in Precambrian marine settings are direct oxidation by anoxygenic photosynthesis (Kappler and Straub, 2005; Konhauser et al., 2002), photocatalytic oxidation by UV radiation (Braterman et al., 1983), and abiotic or biologically-catalyzed reaction (Cloud and Licari, 1968).

Geochemical evidence indicates that the first significant rise in global atmospheric oxygen occurred between 2.4 and 1.8 Ga, commonly referred to as the Great Oxidation Event (GOE) (Anbar et al., 2007; Farquhar and Wing, 2003; Kendall et al., 2010; Lyons et al., 2014; Ostrander et al., 2019, 2021, 2024; Planavsky et al., 2014; Rasmussen and Buick, 1999). This oxygenation event may have facilitated large-scale deposition of banded iron formations (BIFs) via direct

* Corresponding author. Birbal Sahni Institute of Palaeosciences, Lucknow, Uttar Pradesh, India.
E-mail address: a.h.ansari@bsip.res.in (A.H. Ansari).

https://doi.org/10.1016/j.eve.2025.100073
Received 3 May 2025; Received in revised form 4 July 2025; Accepted 23 July 2025
Available online 24 July 2025

oxidation of ferrous iron. Sulfur isotope data, particularly mass-independent fractionation, suggest that the Earth's atmosphere prior to the GOE was largely anoxic (Farquhar and Wing, 2003). Isotopic signatures of elements such as Fe, Mo, S, Ca, and Mg from carbonates and black shales in China, Australia, and South Africa indicate the possible presence of localized oxygen-rich 'oases' in shallow marine settings before the GOE (Luskin et al., 2019; Ostrander et al., 2019, 2021; Peng et al., 2022; Slotznick et al., 2023). However, the extent to which these oxygen oases contributed to BIF deposition via direct oxidation remains uncertain. Notably, laboratory-based experiments have shown that photochemical processes alone are insufficient to account for BIF formation (Konhauser et al., 2007). In contrast, microbial Fe^{2+} oxidation by anoxygenic photoautotrophs is considered a more plausible mechanism for BIF deposition under the anoxic conditions that likely prevailed during the pre-GOE interval (Konhauser et al., 2002; Posth et al., 2008; Walter et al., 2014).

Well-preserved microfossils from BIFs older than the Paleoproterozoic are generally rare worldwide (Lepot, 2020). Well-preserved microfossils from Paleoproterozoic Banded Iron formations have been known for more than a hundred years (Broderick, 1919; Gruner, 1922, 1924; Harder, 1919; Leith, 1903; Moore, 1918). However, the study by Barghoorn and Tyler (1965) garnered major attention since they conducted the first systematic examinations and identified the twelve least ambiguous species of filamentous, spheroidal, and ellipsoidal fossils. Their study was supported by further palaeontological investigations led by Cloud (1965) and Cloud and Hagen (1965). These filamentous (e.g., *Gunflintia minuta*) and coccoid (e.g., *Huroniospora* sp.) microfossils generally associated with the iron-rich Precambrian sedimentary rocks, were hypothetically interpreted to have a role in iron oxidation (Barghoorn and Tyler, 1965; Harder, 1919; Lepot et al., 2017; Shapiro and Konhauser, 2015; Walter et al., 1976). It has been suggested that spheroidal microfossils belonging to the genus *Huroniospora* are either cyanobacteria (Barghoorn and Tyler, 1965) or heterotrophs (Strother and Tobin, 1987). According to a more recent study by Lepot et al. (2017), spheroidal *Huroniospora* and other Paleoproterozoic Gunflint microbiota were Fe-tolerant oxygenic photosynthesizers that could biomineralize iron inside cells.

The taxonomic ramifications of these fossils are crucial because the preservation of bacteria that oxidize Fe^{2+} would help address important issues regarding the genesis of iron formation and offer an intriguing narrative in a pivotal period of Earth's history–the oxygenation of the atmosphere (Bekker and Eriksson, 2003; Bekker et al., 2010; Posth et al., 2013). The palaeontological record between the Great Oxidation Event, which occurred 2.4 billion years ago (Ga), and the final Palaeoproterozoic iron formations, which were deposited 500–600 million years later, is dominated by problematic microfossils (Lepot et al., 2017). Though their affinities, metabolism, and contributions to Earth surface oxidation and Fe deposition are unknown, these fossils are frequently linked to iron-rich sedimentary strata.

Here, we study a recently well-dated 2.85 Ga (Mesoarchean) BIF of the Girar Formation exposed near Baraitha, in Madhya Pradesh, India (Mukhopadhyay, 2020; Slabunov et al., 2024) for micropaleontology and geochemistry. This BIF section shows excellent preservation of solitary and aggregated spheroidal microfossils, which in morphological features and size are similar to the genus *Huroniospora,* convincingly described in many previous studies mainly from Paleoproterozoic sections (Barghoorn and Tyler, 1965; Cloud and Licari, 1968; Knoll and Simonson, 1981; Lanier, 1989; Strother and Tobin, 1987; Walter et al., 1976; Yun, 1984) less convincing from Meso–Neoarchaean the Bababudan Iron Formation in South India (Viswanathiah and Venkatachalapathy, 1980), and the Soudan Iron Formation in North America (Cloud and Licari, 1968).

2. Geological settings and age

The Indian subcontinent hosts five major Archean cratons: the Bundelkhand and Aravalli Cratons lie north of the Central Indian Tectonic Zone (CITZ), and the Dharwar, Singhbum, and Bastar Cratons lying south of the CITZ. The Bundelkhand Craton (Fig. 1) is predominantly composed of K-rich Neoarchean granitoid, intruding into the tonalite trondhjemite granodiorites (TTGs) and greenstone complex of Paleo-Mesoarchean age (Joshi et al., 2017; Kaur et al., 2014, 2016; Mondal et al., 2002). There are three distinct regions within the Bundelkhand Craton: Northern, Central, and Southern Bundelkhand. The Central and Southern Bundelkhand terrains are usually home to greenstone belt complexes associated with the Banded Iron Formation (BIF) (Singh et al., 2021).

The Central Bundelkhand terrain preserves remnants of Paleoarchean (3.4–3.2 Ga) mafic–ultramafic complexes (Singh et al., 2019) and hosts the extensive Meso-to Neoarchean Central Bundelkhand Greenstone Complex, which extends over 150 km. This complex includes the Babina and Mauranipur greenstone belts, along with a small fragment enclosed within granitoids (Malviya et al., 2006, 2022; Singh and Slabunov, 2015, 2016; Slabunov and Singh, 2019). Lithologically, the greenstone complex is subdivided into two stratotectonic associations. The earlier association comprises (1) ultrabasic to metabasalts, (2) metavolcanic rhyolites and dacites, and (3) banded iron formations (BIFs), while the later association consists predominantly of felsic volcanics and BIFs. All units and associations are juxtaposed along tectonic contacts (Singh and Slabunov, 2015; Slabunov and Singh, 2019).

Structurally, the Central Bundelkhand Greenstone Complex represents a tectonic collage in which the constituent lithologies have undergone multiple episodes of metamorphism. Geochronological data indicate that felsic volcanic rocks from the early and late associations crystallized during the Mesoarchean (~2.81 Ga) and Neoarchean (2.54–2.56 Ga), respectively (Singh and Slabunov, 2015; Slabunov and Singh, 2019). Evidence for early accretion is provided by amphibolite-facies metamorphism under elevated pressure conditions, while collisional processes have been dated to between ~2.70 and 2.43 Ga (Saha et al., 2011; Slabunov and Singh, 2021). The most recent metamorphic overprint, corresponding to prehnite–pumpellyite facies associated with rift-related tectonism, is dated to the Paleoproterozoic (1.9–1.8 Ga) (Colleps et al., 2021; Sibelev et al., 2021a, 2021b).

The Southern Bundelkhand terrain is predominantly composed of Neoarchean K-rich granites, with subordinate occurrences of greenstone lithologies represented by the Girar Greenstone Belt, as well as mafic–ultramafic layered and gabbroic intrusions, tonalite–trondhjemite–granodiorite (TTG) suites, and sanukitoids. Recent investigations in this region have identified two large gabbro–diorite intrusions and a Mesoarchean mafic–ultramafic lopolithic body known as the Ikauna Complex (Hiloidari et al., 2021; Ramiz and Mondal, 2017; Singh et al., 2019; Singh and Slabunov, 2016; Slabunov et al., 2017, 2018).

Using the Sm-Nd isochron, Hiloidari et al. (2021) have calculated the age of the metavolcanics (basalt) from Girar to be 2.99 Ga. U-Pb zircon geochronology zircon separated from the Girar BIF yielded an age of 2850 Ma (Slabunov et al., 2024). According to Hiloidari et al. (2021), the Girar greenstone belt is composed of two formations: 1) quartzites and 2) BIFs with interlayered basalts in the southern portion of the belt. Both the BIF and the Girar belt quartzite/BIF boundary are composed of hematite and quartz with substantial bedding (Figs. 1–3). Quartzites are characterized by thick schist (meta-argillite) laminae, smaller quartz pebble conglomerates, and low-grade metamorphism of fuschite, chromite, and hematite-bearing quartz arenite (Slabunov et al., 2017). It was proposed that the 3.43 and 3.35 Ga zircons found in the Girar belt quartzite were derived from the preceding crust, most likely TTG (Slabunov et al., 2017). According to a recent study, Mesoarchean (2.99 ± 0.19 Ga) arc-type basalt is linked to the BIFs in the Girar region (Hiloidari et al., 2021).

Slabunov et al. (2024) geochemical study suggested that the detrital components of BIFs in the Bundelkhand craton were derived from terrigenous mafic and felsic sources. They also found that the

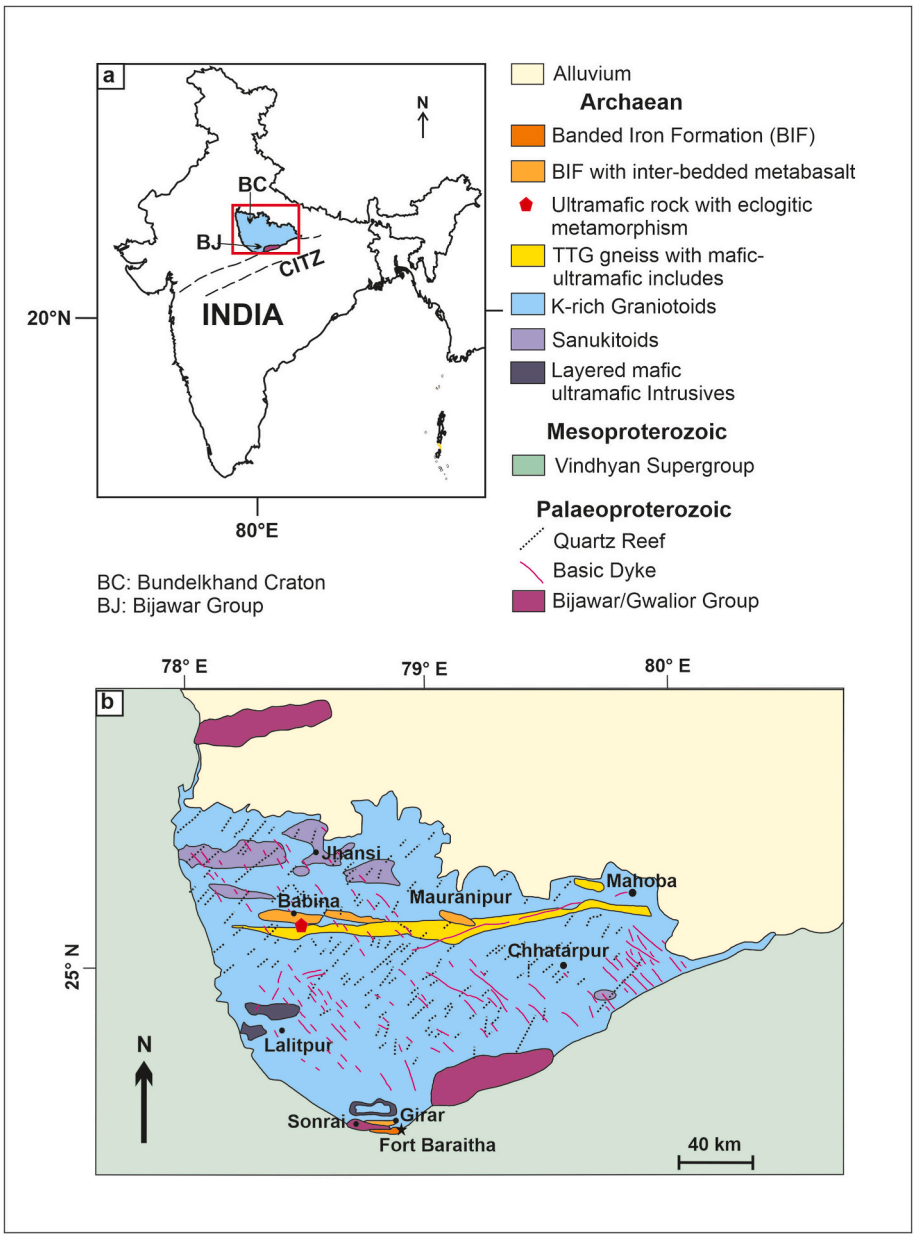

Fig. 1. (a) Map of India highlighting the Bundelkhand Craton (BC). CITZ represents the Central Indian Tectonic Zone. (b) Detailed view of BC, showing the BIF sampling site at the Ruin Fort Baraitha location (marked by a star) (Sibelev et al., 2021a; Slabunov et al., 2024).

geochemical characteristics of these BIFs are similar to other contemporary BIFs from different paleogeographic positions. Neodymium isotope data (εNd = −6.57 ‰–3.45 ‰, average value = 0.01 ‰) from the Bundelkhand BIFs suggest that the iron incorporated into these Iron formations was derived from two primary sources: (1) continental crustal inputs and (2) submarine hydrothermal activity.

These lithologies are traversed by NW trending mafic dykes swarms and NNE–SSW and NE-SW trending quartz veins (reefs) that represent the last magma-related hydrothermal activity in the Bundelkhand Craton (Mondal and Ahmad, 2001; Pati et al., 2007). Based on U-Pb zircon ages, Slabunov and Singh (2022) proposed that the quartz veins formed between ca. 1.87–1.78 Ga. The quartz vein was probably emplaced owing to ongoing crustal movements after stabilizing the cratonic segment at ca. 2.5 Ga. Some believe these results come from shear zones within granitic rocks (Roday et al., 1995), while Pati et al. (2007) suggest the role of late-stage hydrothermal process for their origin. The mafic dykes were emplaced at two discrete time intervals along two prominent orientations: along NW–SE at 2.0 Ga, and along the ENE–WSW at 1.1 Ga (Pradhan et al., 2012) from an enriched mantle source (Mondal and Ahmad, 2001).

3. Methodology

3.1. Sampling

A total of five BIF samples from roughly 20 cm vertical intervals were collected from horizontally laminated facies of a 1-m-thick section of the Girar BIF near ruin Fort Baraitha (24°17′34.598″ N; 78°56′31.819″ E), Chhatarpur District, Madhya Pradesh (Figs. 1–3). The collected samples were prepared and processed for thin sections (two longitudinal sections and two horizontal sections of 30–40 μm thick) at the BSIP Section Cutting Laboratory to perform petrography (using Leica DM2700 P LED polarising microscope) and FESEM studies. The BIF samples were also processed for the trace elements and organic isotope analysis. Carbonaceous microfossils were extracted using the standard acid maceration technique described by Grey (1999).

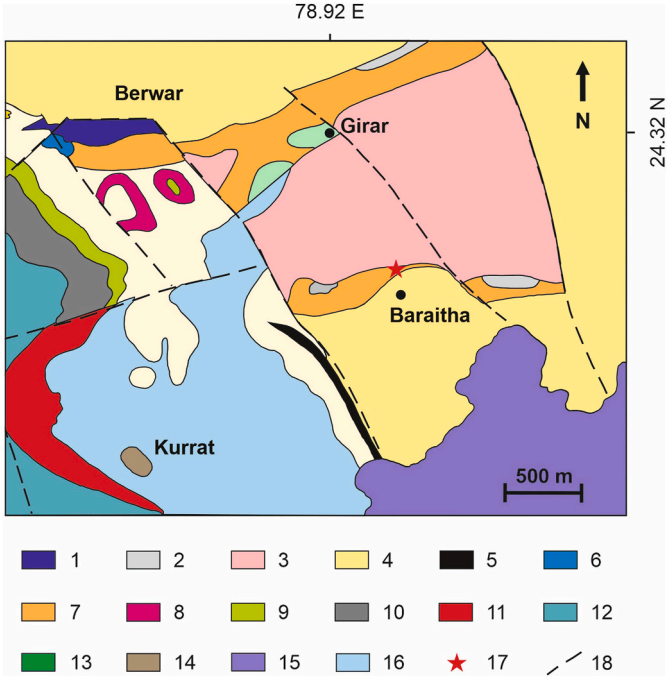

Fig. 2. Geological map of the area between Baraitha-Girar and Dhori, showing the distribution of various lithological units and structural features (Roday et al., 1990). The numbered units are as follows: 1. Quartzite, slates, and fuchsite quartzite; 2. Banded magnetite quartzite and magnetite slates; 3. Metabasic rocks; 4. Granites; 5. Basal Bijawar conglomerates; 6. Jamuni carbonate; 7. Brecciated ferruginous quartzite; 8. Carbonaceous shales; 9. Bandai shales; 10. Rohini carbonate; 11. Pillowed tholeiites; 12. Dhori-Sagra and Soda quartzite; 13. Banded Iron Formation (BIF); 14. Basal Vindhyan conglomerate; 15. Vindhyan quartzite; 16. Alluvium lithofacies; 17. Sampling site (Fort Baraitha); and 18. Faults.

3.2. Field Emission Scanning Electron Microscopy (FESEM)

Specimens were mounted on copper stubs using carbon tape and subsequently coated with a conductive layer using a JEOL JEC 3000 FC sputter coater. Imaging was performed with a field emission scanning electron microscope (FESEM; JEOL JSM-7610F) at appropriate magnifications.

3.3. Trace elements analysis

Approximately 30 mg of each powdered sample was subjected to a two-step acid digestion procedure for trace element analysis, following protocols adapted from Ansari et al. (2023). In the first step, the sample powder was transferred into a Teflon digestion tube, to which 5 mL of a hydrofluoric acid–nitric acid mixture (2:1 ratio) and 1 mL of perchloric acid were added. The tube was securely capped and heated at 120 °C for 7 h using a Q-block system. After digestion, the cap was removed, and the contents were evaporated to complete dryness. In the second step, 5 mL of a hydrofluoric acid–nitric acid mixture (1:2 ratio) and 1 mL of perchloric acid were added to the same tube. The mixture was again heated and evaporated to dryness under the same conditions. After this step, 2 mL of 5 % nitric acid (HNO_3) was added, and the solution was inspected for clarity. If any solid residue remained, the two-step digestion process was repeated until complete dissolution was achieved. The fully digested solution was then diluted with 2 % HNO_3 to a final volume of 50 mL and stored at 4 °C prior to analysis. Standard reference materials from the United States Geological Survey (USGS)–Cody Shale (SCo-1) and Green River Shale (SGR-1b)–along with procedural blanks, were processed using the same method. Selected samples were analyzed in replicate to ensure data quality, with analytical errors maintained below 5 %. The external reproducibility obtained from the analysis of the geostandards and repeat samples was within the error limit.

3.4. Organic carbon isotope analysis

The analysis of δ^{13}Corg and total organic carbon (TOC) was performed following the protocol described by Ansari et al. (2020) and Agnihotri et al. (2020). Initially, the powdered samples were treated with 10 % hydrochloric acid (HCl) to eliminate residual carbonates. The acid-treated samples were thoroughly rinsed with Milli-Q water, then dried in an oven at 60 °C. Once dried, the samples were re-powdered, weighed, and sealed in tin capsules. These tin capsules were combusted at 950 °C in a high-temperature combustion reactor of an Elemental Analyzer (VARIO ISOTOPE SELECT®) interfaced with an isotope ratio mass spectrometer (IRMS; Precision, Elementar®). During combustion, CuO served as the catalyst. The evolved CO_2 from the organic fraction was purified using a reduction reactor filled with reduced copper granules maintained at 650 °C. Isotopic measurements were calibrated against a set of international and in-house reference standards, as described by Agnihotri et al. (2020). Analytical accuracy was assessed using ACA (ε-Amino-n-Caproic acid [$C_6H_{15}NO_2$]), a primary standard calibrated against IAEA-CH-3, IAEA-CH-6, and an Internal standard (Sulphanilamide). For carbon isotopic measurements, the standard reference was Vienna Pee Dee Belemnite (Vienna-PDB). Analytical precision was routinely monitored through repeated measurements of the laboratory standard 'sulphanilamide', with a reproducibility better than ±0.2 ‰.

TOC content was quantified based on the peak area of the CO_2 chromatogram recorded by the mass spectrometer.

4. Results

4.1. Thin section observations

4.1.1. Petrography

The BIF is composed of multiple bands of variable thickness of chert (microcrystalline quartz) and hematite-rich layers with reddish-brown stains of iron oxide (Fig. 4a and b). Few of the hematite-rich layers also show distinguishingly smaller quartz grains compared to the grains in the chert layer (Fig. 4a and b). Although not widespread, recrystallization of quartz is evident from the XPL section of a large quartz grain in the chert layer (Fig. 4c and d). The recrystallization is a result of diagenesis, as no metamorphic alterations could be seen at the quartz-hematite boundaries that would otherwise form minerals like chlorite, amphibole, or pyroxenes (depending on the metamorphic grade). Also, there are no signs of crystallized fluid veins that could have caused significant alterations. We also observe a few large hematite grains that are euhedral with a distinct hexagonal outline (Fig. 4c and d).

4.1.2. Micropaleontology

The thin-section photograph reveals a dense aggregation of rounded to sub-rounded structures, predominantly exhibiting spherical morphologies (Fig. 5a–e). These structures are uniformly small, measuring 1.7–9.3 μm (mode value = 5.4 μm, n = 600) in diameter, as inferred from the scale bar (Fig. 5a–e). The spheroids are arranged in clusters, with localized areas of high density interspersed with clearer regions. The outlines or walls of the spheroids are generally thick and sharp. The coloration of the microfossils is dominated by reddish and orange hues (Fig. 5a–e). The surrounding matrix appears fine-grained and light. From a taphonomic perspective, the structures appear moderately to well-preserved, retaining their original spherical forms despite evidence of mineral overprinting. The spheroidal clusters are found mainly associated with the rich silica precipitates (Fig. 5a–e).

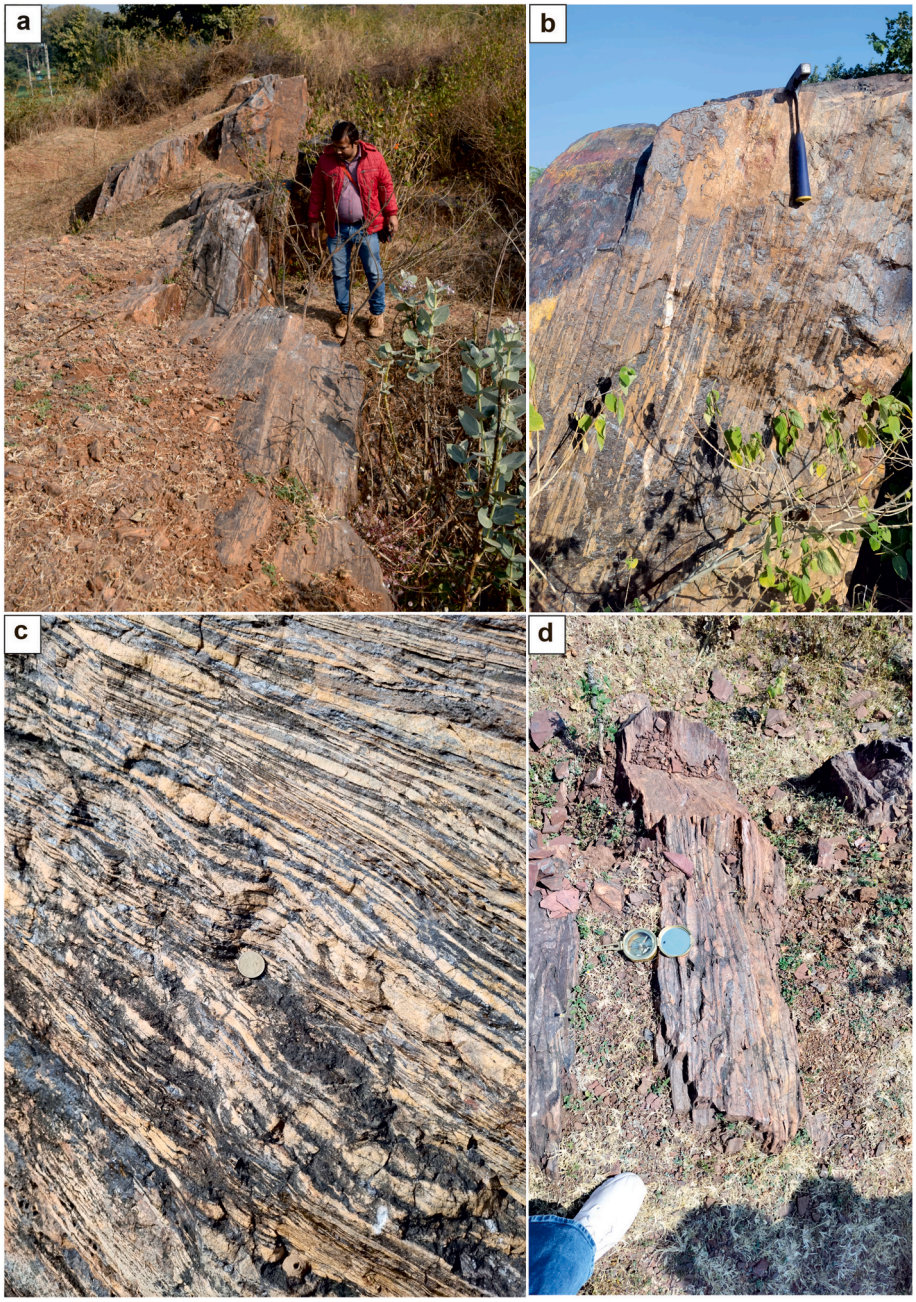

Fig. 3. (a) Field view of the Girar-Baraitha Banded Iron Formation (BIF) exposure; the person in the image (height = 162 cm) provides scale. (b–d) Close-up photographs of the Girar-Baraitha BIF showing well-defined alternating dark and light bands, interpreted as iron-rich and silica-rich layers, respectively. Scales shown include a geological hammer (30 cm in length), a 5 Rupees coin (2.3 cm diameter), and a field compass (8 cm diameter).

4.2. Carbonaceous microfossils isolated through acid maceration

4.2.1. High-power microscopy

The microfossils in the image exhibit a complex and varied morphology. The overall structure consists of irregularly shaped clusters (Fig. 5f–i), with individual sub-units displaying spherical to subspherical shapes. Some edges appear angular or fragmented. The surface texture of the microfossils is granular to amorphous, with certain areas showing smoother sub-units. This granular appearance could indicate micro-crystalline or organic material, while the smoother portions may represent preserved internal structures, such as cell walls or sheaths (Fig. 5f–i). Additionally, some translucent regions in their interstitial spaces can be seen. The presence of stratified or layered features (overlapping of spheroids) in the cluster is also present (Fig. 5f–i).

In terms of coloration, the microfossils range from light to dark brown tones. This variation in opacity reflects heterogeneity in the composition or preservation levels of the microfossils. The scale bar in the image reveals that the spheroid diameter ranges from approximately 1–5 μm (Fig. 5f–i), which is consistent with spheroids observed in the thin section (Fig. 5f–i).

4.2.2. Scanning electron microscopy (SEM)

The microfossil in the SEM image exhibits a complex, three-dimensional structure with a cauliflower-like or botryoidal shape (Fig. 6a–d). It appears to be composed of numerous spherical or ovoid structures closely packed together, forming a larger, irregular mass. Using the 10 μm scale bar as a reference, the overall diameter of the microfossil cluster is estimated to be around 50–60 μm (Fig. 6a and b).

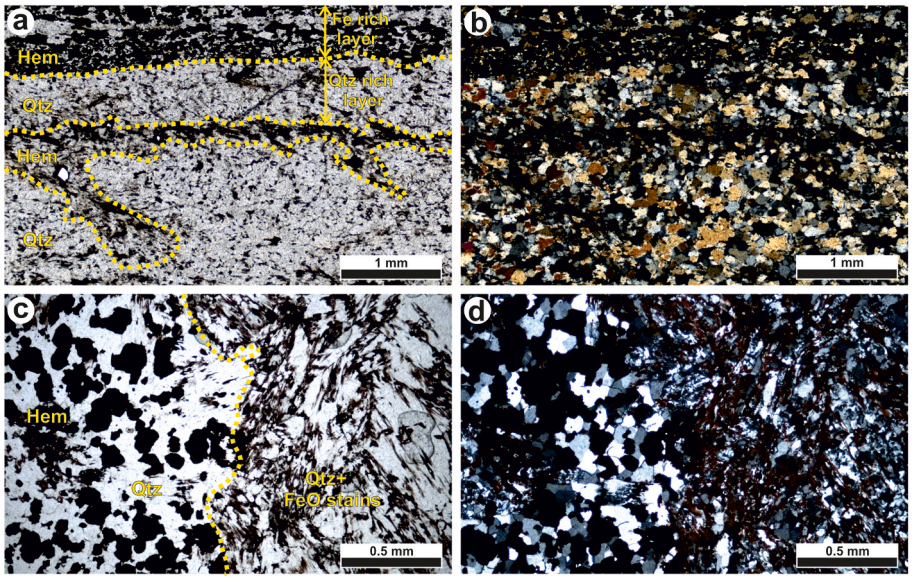

Fig. 4. Microscopic images of BIF (a, b) showing bands of white quartz-rich layers and dark iron oxide-rich layers in (a) PPL and (b) XPL; (c, d) showing subhedral to euhedral crystals of hematite grains in relatively large microcrystalline quartz grains and iron stain-rich layer in finer microcrystalline quartz in (c) PPL and (d) XPL.

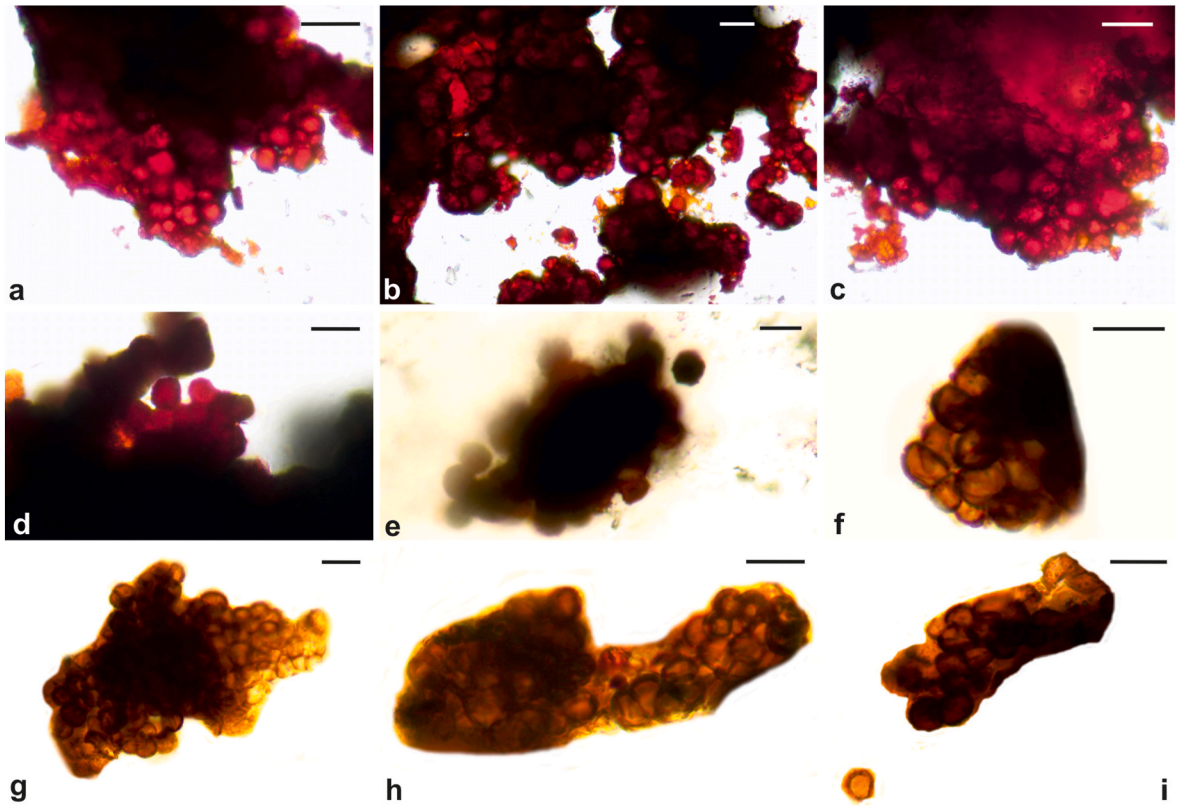

Fig. 5. (a–e) Thin-section images showing spheroidal microfossil aggregates appearing red due to oxidized iron. The spheroidal microfossils range from 1 to 9 μm in diameter. (f–i) Carbonaceous spheroidal microfossil aggregates isolated using the acid maceration technique, with diameters also ranging from 1 to 9 μm. All scale bars represent 10 μm.

The individual spherical structures within the cluster appear to have a diameter of approximately 5–10 μm, with some variation in size (Fig. 6a–d). The surface of the cluster is rough and uneven, with numerous bumps and projections. Individual spherical structures within the cluster are visible, with some appearing to have a distinct cell wall or boundary (Fig. 5c and d). The surface of the individual units is not perfectly smooth but may exhibit fine surface ornamentation or textures. There are also visible pores or openings on the surface of the microfossil (Fig. 5a–c, d).

The presence of a distinct cell wall or boundary around individual spherical structures is evident. The cell wall appears to be relatively thick (thickness between ~ 285 nm and ~450 nm) and may have a complex structure (Fig. 5a), possibly with multiple layers or ornamentation. The thickness and structure of the cell wall might vary between

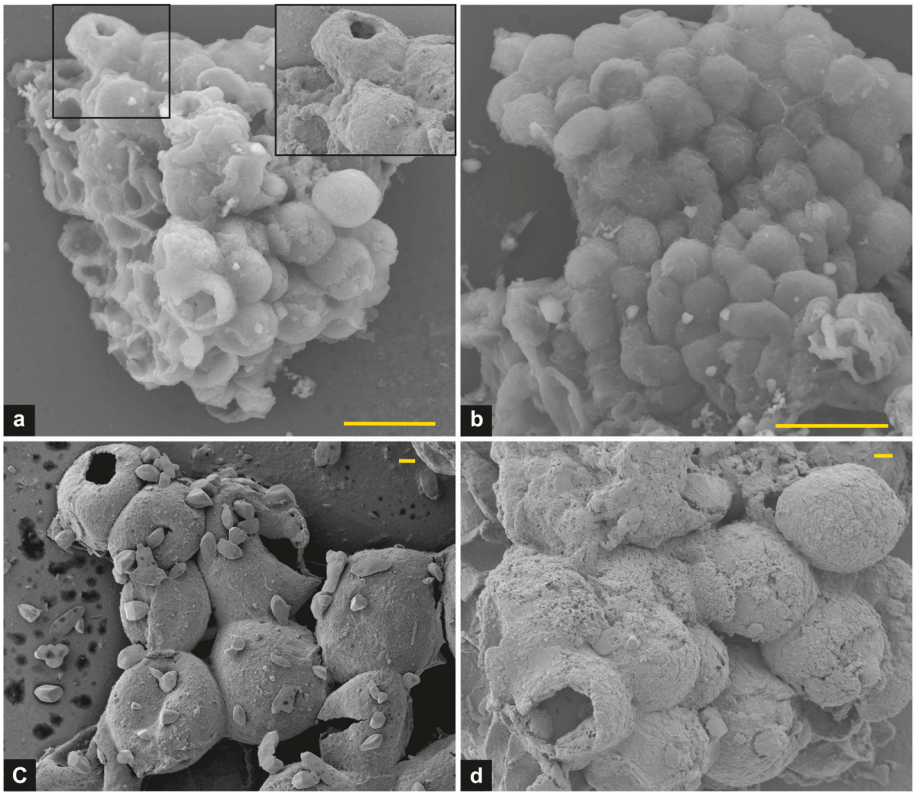

Fig. 6. (a–d) SEM images depicting the detailed three-dimensional morphology of spheroidal microfossil aggregates. (a, c, d) images show the presence of an aperture at one pole of the spheroid.

different cells within the colony. These internal structures might include vacuoles, organelles, or other cellular components.

4.3. Trace elements geochemistry and organic carbon isotope

Trace element results of the Girar-Baraitha BIF are listed in Table 1. Detrital elements such as Sc, Ti, and Zr are depleted compared to PAAS values, and redox-sensitive trace elements such as Mo, Cr, and U show enrichment more than 130, 250, and 6.8 times, respectively (Table 1). The cross plot between Sm/Yb vs Eu/Sm shows the mixing of hydrothermal fluid with seawater in a ratio from 1:1000 to 1:100 (Fig. 5c). The Ce/Ce* anomaly calculated from PASS normalized REE data (equation for $Ce/Ce^* = Ce/\sqrt[2]{La \times Pr}$) shows that all five sample data fall in Zone IIa, which is characterized by no cerium anomaly and no lanthanum anomaly (Fig. 7a).

The PAAS normalized REE + Y of the Girar-Baraitha BIF shows similarity with that of an earlier study of the Girar BIF from a different location (Fig. 7b). In this study, Girar BIF shows a consistently high Europium anomaly (equation for $Eu/Eu^* = Eu/\sqrt[2]{Sm \times Gd}$) ranging from 2.3 to 2.8 (average = 2.53) and Pr/Pr* anomaly [equation for $Pr/Pr^* = 2 \times Pr/(Ce + Nd)$] ranges between 0.94 and 1.00. The Y/Ho ratio for the Girar-Baraitha BIF ranges between 27.7 and 31.7 and shows a statistically significant ($p < 0.05$) negative correlation with Zr (Fig. 8).

The δ^{13}C-org values for Girar-Baraitha BIF ranged from −27.8 ‰ to −35.2 ‰ with an average value of −31.9 ‰ (Table 2 and Fig. 9). TOC in these samples ranges between 0.01 % and 0.03 % (Table 2).

5. Discussions

5.1. Morphology, preservation, and biological significance of microfossils in the Girar-Baraitha BIF

The overall structure consists of irregularly shaped clusters, with individual sub-units displaying spherical to subspherical shapes, possibly indicating coccoidal forms. Some edges appear angular or fragmented, likely due to diagenetic alteration. The clustered arrangement suggests biological remnants, such as microbial colonies, and highlights a possible biological origin for these microfossils. The scale bar in the image reveals that the sub-units range from approximately 1.7–9.3 μm (Figs. 5 and 6), which is consistent with bacterial cells and fungal spores. The surface texture of the microfossils is granular to amorphous, with certain areas showing smoother sub-units (Fig. 6). This granular appearance could indicate organic material, while the smoother portions may represent preserved internal structures, such as cell walls or sheaths. The presence of stratified or layered features hints at successive growth phases over time. This remarkable preservation of microfossils in the Girar-Baraitha BIF succession could be due to two possible reasons: 1) this succession shows limited alteration; 2) the high silica content (up to 85 %) (Slabunov et al., 2024) likely contributed to the long-term preservation of these microfossils by providing a protective matrix.

The SEM image reveals a high level of preservation detail, suggesting that the microfossil has been well-preserved. The three-dimensional structure is visible, indicating minimal deformation during fossilization (Fig. 6). There is no apparent significant deformation or distortion of the microfossil. The microfossil appears to be preserved as a complete cluster, indicating that there was minimal disarticulation during fossilization. This indicates rapid burial and protection from significant physical or chemical alteration. The cell wall appears to be relatively thick and may have a complex structure, possibly with multiple layers. The thickness of the cell wall might vary between different cells (Fig. 6). The cell walls appear to be closely adpressed to each other, suggesting strong intercellular connections (Fig. 6). The presence of a distinct cell wall further supports the interpretation of individual spherical structures as cells. The presence of pores or openings suggests a complex life cycle and potential interactions between cells within the colony.

Table 1
The concentration of trace elements (in ppm) and enrichment of Mo, Cd, Cr, and Se relative to PAAS in the Girar-Baraitha BIF.

Elements	BIF-1	BIF-2	BIF-3	BIF-4	BIF-5
Sc	1.39	0.67	0.65	0.40	0.41
Ti	118.92	46.27	66.54	71.16	27.39
V	12.33	11.66	31.95	7.13	2.73
Cr	192.95	183.50	205.93	185.83	191.00
Mn	30.72	192.98	123.26	63.70	50.36
Co	206.71	126.90	86.58	156.93	76.14
Ni	21.11	28.69	25.00	20.85	21.19
Cu	50.44	46.71	12.64	55.43	17.95
Zn	24.31	15.38	13.19	16.80	21.12
Se	0.46	1.57	0.82	1.30	0.33
Rb	0.77	0.20	0.13	0.17	0.39
Y	1.81	3.66	1.45	1.24	1.28
Zr	3.69	1.53	2.61	1.84	2.22
Mo	1.35	1.17	1.64	0.96	1.13
Cd	0.02	0.01	0.02	0.01	0.02
Mo_{EF}	64.26	134.18	110.02	91.77	89.04
Cd_{EF}	10.29	14.70	14.43	10.66	15.54
Cr_{EF}	109.77	251.56	165.21	212.04	180.13
Se_{EF}	268.90	2199.97	673.45	1515.62	318.03
La	1.65	3.01	1.72	2.54	1.18
Ce	3.28	5.92	2.85	4.51	2.49
Pr	0.38	0.69	0.37	0.54	0.31
Nd	1.67	3.06	1.61	2.20	1.32
Sm	0.37	0.70	0.33	0.41	0.26
Eu	0.21	0.45	0.18	0.23	0.15
Gd	0.42	0.79	0.40	0.41	0.33
Tb	0.05	0.09	0.05	0.04	0.04
Dy	0.35	0.59	0.26	0.23	0.22
Ho	0.07	0.12	0.05	0.04	0.04
Er	0.20	0.36	0.15	0.13	0.13
Tm	0.03	0.05	0.02	0.02	0.02
Yb	0.20	0.38	0.15	0.12	0.13
Lu	0.03	0.05	0.02	0.02	0.02
Th	0.24	0.14	0.17	0.11	0.12
U	0.21	0.11	0.21	0.18	0.20

Additionally, a fine-grained matrix surrounding the object suggests mineral precipitation occurred during burial. The preservation of the carbonaceous microfossils (mostly spheroidal) is mostly found associated with the light-colored silica-rich matrix (Fig. 5a–e). Whereas, the dark-colored iron oxide-rich matrix contains a relatively much lesser fraction of carbonaceous matter.

The clustered arrangement of spheroids in the Baraitha-Girar BIF suggests that these microfossils may represent biological remnants, such as fossils of microbial colonies preserved at the cellular level. Their morphology closely resembles that of petrified prokaryotes, particularly colonial coccoid cyanobacteria. Similar microfossils with comparable shapes and sizes have been reported from various Proterozoic strata (Barghoorn and Tyler, 1965; Cloud and Licari, 1968; Knoll and Simonson, 1981; Lanier, 1989; Lepot et al., 2017; Strother and Tobin, 1987; Walter et al., 1976; Yun, 1984). Individual spheroids from the Giara-Baraitha BIF show the closest resemblance to the genus *Huroniospora* in terms of thickness, size, and shape (Barghoorn and Tyler, 1965). Additionally, the presence of an aperture at the constricted ends of ellipsoidal bodies (Fig. 6a–c, d), noted in the original generic description of *Huroniospora* (Barghoorn and Tyler, 1965), is also observed in some individuals from the Girar-Baraitha BIF, where clusters show a defined opening/aperture. *Huroniospora* is typically found in solitary (Barghoorn and Tyler, 1965) occurrences and rarely in colony (Lanier, 1989), whereas the spheroids in the Giara-Baraitha BIF are primarily colonial.

Alternatively, colonies of spheroidal microfossils in Girar-Baraitha BIF can be compared with the genus *Corymbococcus* (Awramik and Barghoorn, 1977), which is also only reported in the Proterozoic successions, but is rarely compared to the genus *Huroniospora* (Sergeev and Seong-Joo, 2004). This genus consists of colonial clusters of unicells, each measuring 5–18 μm and typically spherical or slightly ellipsoidal, enclosed within a shared, non-lamellated envelop (Awramik and Barghoorn, 1977). The individual cells, when stripped of their envelopes or sheaths, closely resemble those of the genus *Huroniospora*. However, *Corymbococcus* is primarily colonial with a wall thickness relatively larger (1.5 μm thick) compared to *Huroniospora* [wall thickness 110–600 nm (Lepot et al., 2017)], and the spheroidal microfossils of Girar-Baraitha BIF [wall thickness (~300 nm)]. The thickness of cell walls, along with intricate internal wall structures, can be preserved in the rock record with diagnostic fidelity (Javaux et al., 2004). However, it has been proposed that the thick-walled variants of these microfossils may have originated through early diagenetic accumulation of organic material onto thin-walled *Huroniospora* (Strother and Tobin, 1987). The three-dimensional preservation of microfossils necessitated silica encapsulation and impregnation, processes that likely left insufficient space for the substantial (threefold to tenfold) increase in wall thickness required for such a transformation (Campbell et al., 2015). Lepot et al. (2017) argued that the lack of overlap in the wall thickness indicates that thicker-walled forms could not have arisen from the thickening of their thinner-walled counterparts. Consequently, the significant disparity in wall thickness suggests the existence of distinct precursor wall structures.

Huroniospora and *Corymbococcus* both are absent in Archean rocks. However, in a paleontological study of banded ferruginous quartzites from the Bababudan belt of the Dharwar Craton, Viswanathiah and Venkatachalapathy (1980), found solitary spheroidal microfossil aligned to the characteristic shape of *Huroniospora* but of a slightly larger size (23–30 μm). Colonies of spheroidal microfossils of similar diameter (5–60 μm, mostly <15 μm) have been reported from Archean age (~3.4 Ga old) Strelley Pool Formation, Gorge Creek Group in the Pilbara Craton, Australia (Sugitani, 2019), and Kromberg Formation (~3.4 Ga old) in Barberton Greenstone Belt, South Africa (Kremer and Kaźmierczak, 2017). But, unlike *Huroniospora* as well as spheroidal microfossil in Girar-Baraitha BIF, in which thin section study showed a clear distinction between dark colored cell wall and light-colored interior part of the cellular body (low density of carbonaceous matter), the spheroidal microfossils reported from Strelly Pool Formation, Gorge Creek Group, and Kromberg Formation show no clear distinction between the dark-colored cell wall and dark colored interior part of the cellular body. Also, unlike the early studies (Barghoorn and Tyler, 1965; Knoll et al., 1988; Lepot et al., 2017; Strother and Tobin, 1987), which have demonstrated both thin-walled (40–60 nm) and thick-walled (110–600 nm) coexisting morphospecies of *Huroniospora*, the spheroidal microfossils of Girar-Baraitha BIF show uniformly thick walls.

The spheroidal microfossils identified in the Girar-Baraitha BIF exhibiting a remarkable morphological fit with the thick-walled morphospecies of *Huroniospora* in terms of size, shape, and wall structure, represent the oldest known record of well-preserved *Huroniospora*-like microfossils. However, unlike in younger deposits (Lanier, 1989), *Huroniospora* colonies in Girar-Baraitha BIF do not show any sign of mucilaginous sheaths. This colonial habit suggests an early ecological or behavioral adaptation to the iron-rich Archean environment, potentially reflecting a precursor morphospecies similar to *Huroniospora* that thrived in communal structures. The discovery of these microfossils not only extends the geological record of distinct cellular life into the Archean but also provides critical insights into the evolutionary origins and ecological strategies of early microorganisms in iron-dominated ecosystems. Their presence in such an ancient setting underscores the adaptability of microbial life to extreme environments and highlights the importance of colonial behavior as a potential survival mechanism in Earth's early biosphere.

Several possible affinities have been proposed for *Huroniospora* or *Huroniospora*-like microfossils, including cyanobacteria, iron bacteria, and fungal spores (Barghoorn and Tyler, 1965; Lanier, 1989; Strother and Tobin, 1987; Viswanathiah and Venkatachalapathy, 1980). Targeted nanoscale organic carbon isotope studies of Proterozoic *Huroniospora* by House et al. (2000) and Williford et al. (2013) showed

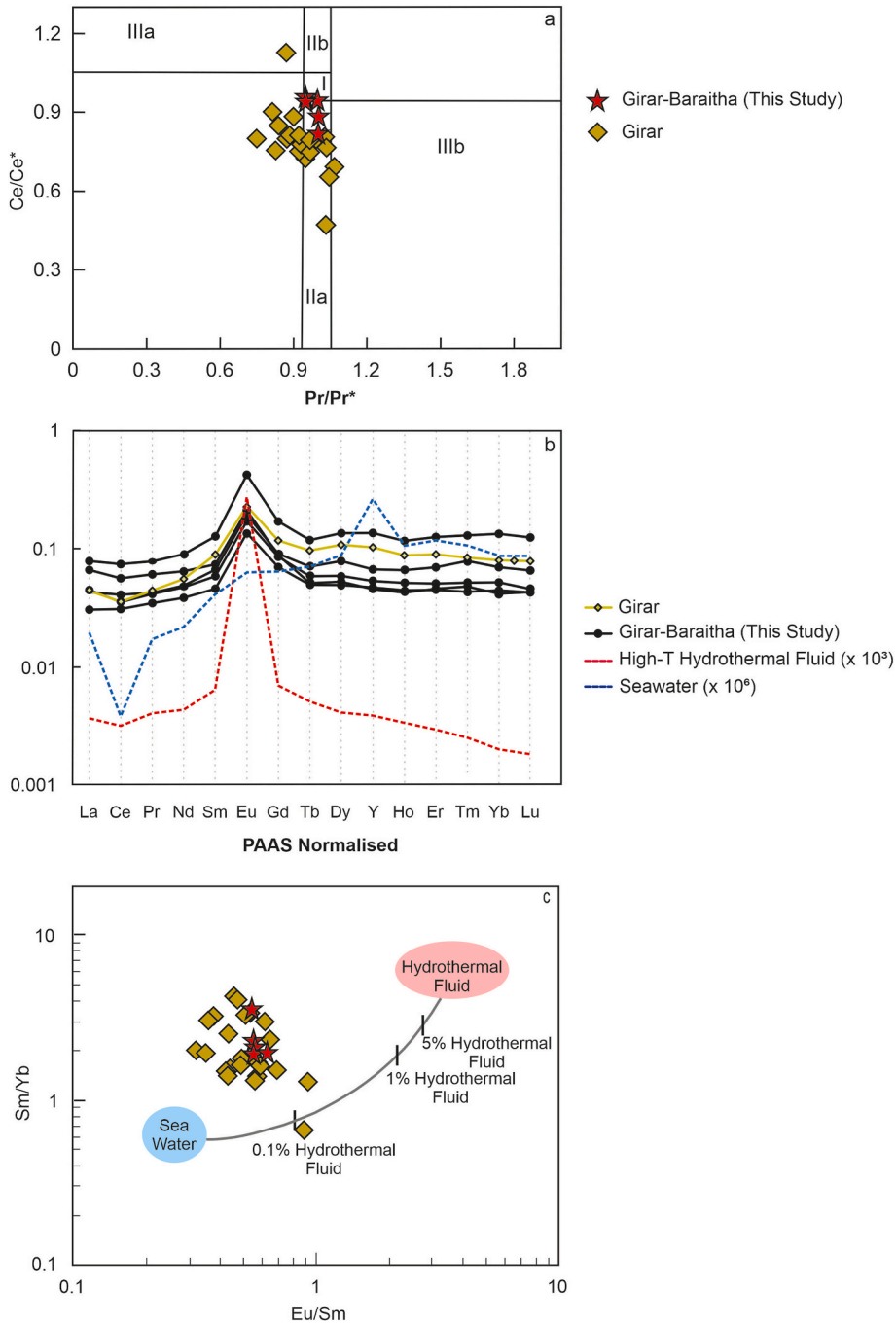

Fig. 7. a) Cerium anomaly vs. Praseodymium anomaly plot for the Girar-Baraitha BIF, along with published data from the Girar, Babina, and Mauranipur BIF (Slabunov et al., 2024), indicating no Cerium or Lanthanum anomaly in the Girar-Baraitha BIF samples. (b) REE + Y pattern of the Girar-Baraitha BIF displaying a significant positive Europium anomaly, closely resembling high-temperature hydrothermal fluids. (c) Sm/Yb vs. Eu/Sm plot illustrating the mixing of hydrothermal fluids with seawater, with a ratio ranging between 1:1000 and 1:100 (Alexander et al., 2008; Alibo and Nozaki, 1999; Bau and Dulski, 1999).

δ^{13}C-org ranging between −29.8 ‰ and −36.5 ‰ (Fig. 9) and attributed it to the Calvin cycle pathway of CO_2 fixation used by cyanobacteria. Our study of the carbon isotope of the bulk organic composition of the Girar-Baraitha BIF samples shows δ^{13}C-org ranging between −27.8 ‰ and −35.2 ‰ (Fig. 9), which is consistent with the reported range. Fig. 6 shows that the δ^{13}C-org range for the Girar-Baraitha BIF significantly overlaps with the anoxygenic δ^{13}C-org range reported for anoxygenic photosynthesizers, methanogenic bacteria, methanotrophic bacteria, eukaryotic algae, and to some extent cyanobacteria whereas showing insignificant overlapping with the range reported for fungi (including fungal spores) (Fig. 9). According to the molecular (Sánchez-Baracaldo et al., 2017) and palaeontological studies (Bengtson et al., 2017; Butterfield, 2000), eukaryotic algae appeared between the late Mesoproterozoic and early Neoproterozoic. This narrows the possible affinities for the *Huroniospora*-like fossils discovered in the Girar-Baraitha BIF to anoxygenic photosynthesizers, methanogenic archaea, methanotrophic bacteria, and to some extent cyanobacteria. This circumstantial evidence indicates anaerobic oxidation of Fe^{2+} to Fe^{3+} as a major pathway for the formation of Girar-Baraitha BIF. Additionally, the organic carbon content in the BIFs from Girar-Baraitha (0.01–0.03 %) is consistent with previous data (Thompson et al., 2019), indicating the presence of chemolithoautotrophic and/or

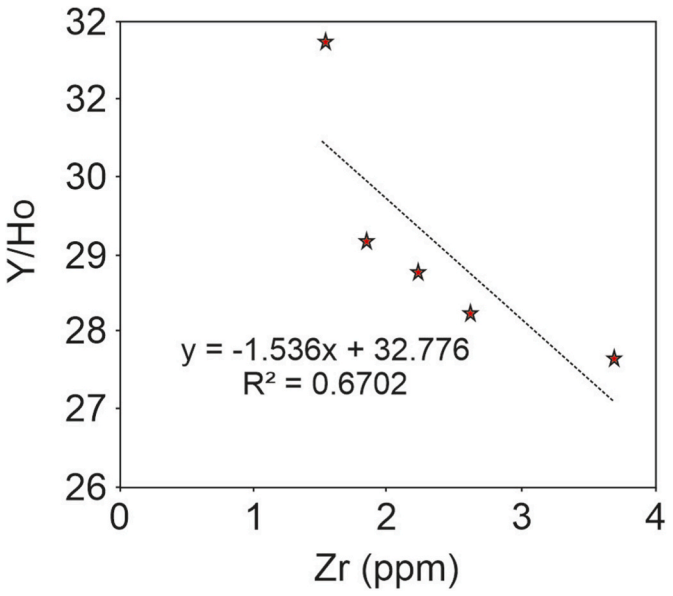

Fig. 8. Y/Ho vs. Zr plot showing a statistically significant negative correlation.

Table 2
δ^{13}C-org and Total organic carbon content (TOC) in the bulk Girar-Baraitha BIF samples. R denotes the repeat analysis.

Sample	TOC	δ^{13}C-org (‰)
BIF-1	0.02	−27.85
BIF-2	0.02	−30.34
BIF-3	0.01	−28.81
BIF-4	0.03	−34.57
BIF-4R	0.02	−34.61
BIF-5	0.02	−35.22

microaerophilic organisms under low-oxygen conditions (Konhauser et al., 2002; Smith et al., 2013).

5.2. Sourcing of Fe^{2+} for the BIF

The PAAS normalized REE profile of Girar-Baraitha BIF shows a lack of negative or positive Ce anomalies but a significant positive Eu/Eu* (Fig. 7a and b). This REE + Y pattern is usual to that found in Pre-GOE BIFs (Alexander et al., 2008; Konhauser et al., 2017; Wang et al., 2024a, 2024b) and can be explained by a combination of contemporary seawater to hydrothermal fluid (Alexander et al., 2008; Alibo and Nozaki, 1999; Barrett et al., 1988; Bau and Dulski, 1999; Dymek and Klein, 1988; Klein and Beukes, 1989). The Sm/Yb vs Eu/Sm plot (Fig. 7b and c) shows the mixing of hydrothermal fluids with the seawater in a ratio ranging between 1:1000 and 1:100 (Fig. 7c). A large positive Eu/Eu* (>2) suggests that the Fe in the Girar-Baraitha BIF was hydrothermally derived because it is generally assumed that Fe and REE + Y will not be fractionated during transport from deep-sea spreading ridges or other exhalation centers due to the high sorption capacity of Fe^{3+}–oxyhydroxides (Danielson et al., 1992; Michard and Albarède, 1986; Slack et al., 2007, 2009). Nevertheless, the erosion of the Eu-enriched Archean continental crust can also raise Eu concentrations (Bolhar et al., 2004; Taylor and McLennan, 1986). It has long been believed that changes in hydrothermal flux are recorded by secular trends in the magnitude of Eu anomalies in large Superior-type BIFs (Bau and Möller, 1993; Danielson et al., 1992; Derry and Jacobsen, 1990; Sreenivas and Murakami, 2005; Viehmann et al., 2015). Comparison of the Girar-Baraitha Eu/Eu* data with the BIF records from the Precambrian period (Fig. 10) indicates that the Girar-Baraitha BIF deposition was associated with an increased influx of the hydrothermal fluids in the global concurrent ocean (~2.85 Ga). High amounts of dissolved Fe^{2+} may have been supported by the anoxic ocean waters of this era.

The Y/Ho ratio of the Girar-Baraitha BIF ranges between 27.6 and 31.7 with an average value of 29.1 (Fig. 8). This average Y/Ho ratio is consistent with the Girar-BIF average (Y/Ho = 31) reported by Slabunov et al. (2024), closely approximates the chondritic values (Y/Ho = 28), but is much lesser than the superchondritic value for the ocean (44–47) (Bau and Dulski, 1999). Y concentrations are conservative in the modern oxidized ocean, where saltwater and hydrothermal fluids mix close to vent orifices. Conversely, when Fe^{2+} starts to quickly oxidize to Fe^{3+} as

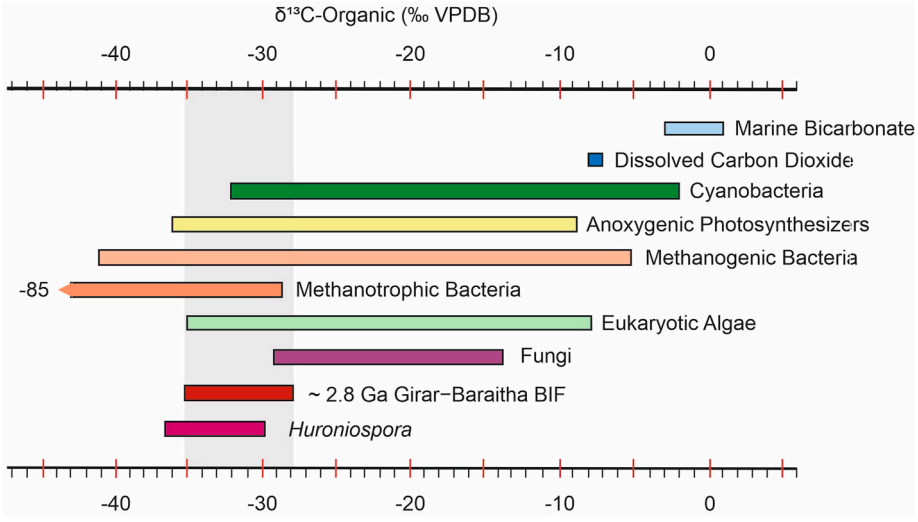

Fig. 9. The δ^{13}C-org values of various potential carbon sources, including marine bicarbonate and dissolved CO_2, alongside biological contributions from anoxygenic photosynthesizers, methanogenic bacteria, and eukaryotic algae (Schidlowski, 2001). Also shown are δ^{13}C-org values for fungi (Courty et al., 2011; Hobbie and Boyce, 2010; Mayor et al., 2009; Ogura-Tsujita and Yukawa, 2008; Suetsugu et al., 2020), *Huroniospora* (House et al., 2000; Williford et al., 2013), and the Girar-Baraitha BIF (this study). This comparison helps assess the potential biological and geochemical sources contributing to the carbon isotopic signature of the Girar-Baraitha BIF.

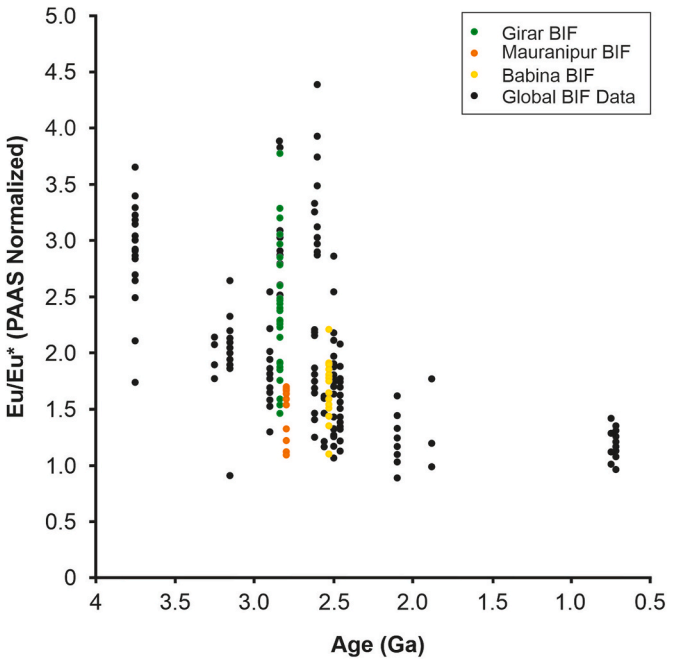

Fig. 10. Post-Archean Average Shale (PAAS)-normalized Europium anomaly variations in BIFs from the Precambrian time frame (Konhauser et al., 2017). Data from the Girar-Baraitha BIF (this study) are plotted alongside published data from the Girar BIF (Slabunov et al., 2024). Additionally, published Europium anomaly data for the Babina and Mauranipur BIFs (Slabunov et al., 2024) are included for comparison. This plot highlights variations in hydrothermal influence across different BIF deposits.

soon as it is released from the vents, precipitating Fe-oxyhydroxides partially adsorbs REEs from the hydrothermal fluids, resulting in a significant drop in sedimentary Y/Ho ratios in comparison to seawater (Bau and Dulski, 1999). Experiments have shown that fractionation in river and estuary systems is minimal and has little effect on the relative abundance of Y and Ho in the ocean, despite the fact that the Y/Ho ratio for rivers and estuaries falls between the values of saltwater and continental rocks (Nozaki et al., 1997). Consistently low concentration of terrigenous detrital-bound conservative elements such as Sc, Zr, and Th in the Girar-Baraitha BIF, suggests low input of terrigenous material in the depositional environment. Hence, the Girar-Baraitha BIF was most likely deposited in an offshore setting close to an active hydrothermal site. However, the Y/Ho ratios exhibit a negative association with Zr (R = 0.670, Fig. 8), which means even though terrigenous detrital input was low, it influenced the real Y/Ho ratio, creating the appearance of a relatively low average Y/Ho ratio. Among the five samples, four of the BIF samples have chondritic ratios (Fig. 8), which are consistent with a hydrothermal origin. In conclusion, a hydrothermal source rather than a terrigenous input is thought to be more closely associated with the provenance of the Girar-Baraitha BIF.

5.3. Fe^{2+}–Fe^{3+} oxidation mechanism

There are four main proposed pathways for the oxidation of Fe^{2+} to Fe^{3+} in pre-GOE oceans: 1) photocatalytic oxidation by UV radiation (Braterman et al., 1983), and 2) direct oxidation by anoxygenic photosynthesis (Konhauser et al., 2002; Kappler and Straub, 2005), 3) direct abiotic oxidation by O_2 produced by oxygenic photosynthesizers (Fig. 11), 4) Paragenesis of greenalite over geological time scale (Nke et al., 2024; Rasmussen et al., 2021).

According to mass-balance calculations and considerations, the amount of oxidants (hydrogen peroxide) that could be produced by UV photo-oxidation of water is found orders of magnitude too small to account for the Fe^{3+} sedimentation needed to form BIF (Pecoits et al., 2015). Therefore, it appears doubtful that UV photooxidation served as the primary mechanism of Fe^{3+} for the deposition of big BIFs, even though it is still feasible that it played a role in IF precipitation.

Although greenalite and other Fe^{2+}-rich phases have been proposed as potential precursors to iron formation (IF) deposition (Nke et al., 2024; Rasmussen et al., 2021), multiple lines of evidence challenge this interpretation (Konhauser et al., 2017; Robbins et al., 2019). The requirement for post-depositional oxidation of Fe^{2+} to Fe^{3+} conflicts with the paragenetic sequence and low-temperature isotopic signatures observed in the Dales Gorge Member (Li et al., 2013), which are inconsistent with high-temperature fluid migration scenarios. Additionally, the experimental pH conditions necessary for greenalite precipitation (7.75–8.3) are not supported by geochemical models of Archean seawater (6.5–7) (Halevy and Bachan, 2017), though they may occur locally during diagenesis. Overall, these constraints argue against greenalite as a primary precipitate in BIFs, supporting Fe^{3+}-oxyhydroxides or Fe^{3+}-Si gels as more plausible primary phases.

Archean oceans are typically suggested to have negligible to no free molecular oxygen before the onset of GOE (Lyons et al., 2014; Planavsky et al., 2010; Warke et al., 2020). However, recent studies (Luskin et al.,

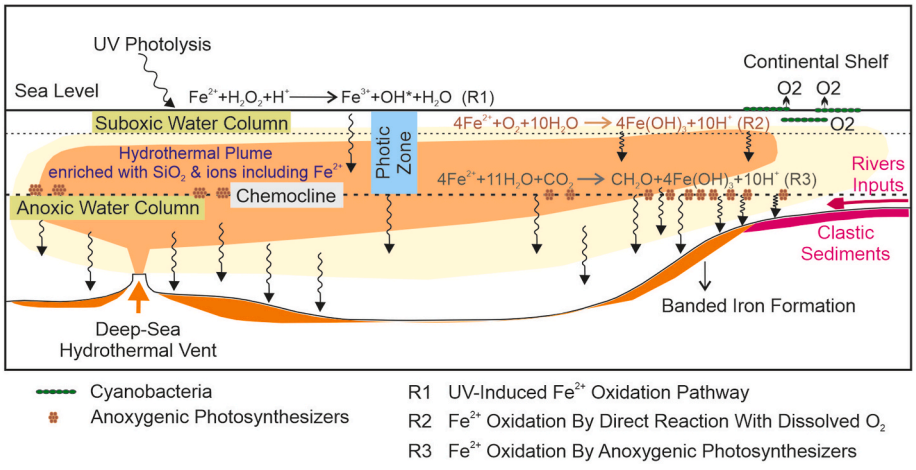

Fig. 11. Schematic model illustrating the possible sources of Fe^{2+} and the potential pathways for its oxidation to Fe^{3+} in the Girar-Baraitha Basin. The model considers hydrothermal inputs, continental weathering, and microbial processes as primary Fe^{2+} sources. Oxidation pathways include abiotic oxidation, oxygenic photosynthesis, and anoxygenic photosynthetic iron oxidation mediated by phototrophic bacteria. This framework provides insights into the redox conditions and biogeochemical cycling of iron in the basin.

2019; Ostrander et al., 2019, 2021, 2024; Peng et al., 2022) have inferred oxygenic photosynthesis occurring on a local scale during pre-GOE. Thus, the question remains open whether Fe^{2+} to Fe^{3+} oxidation was caused by anaerobic phototrophic iron-oxidizing bacteria (Konhauser et al., 2002; Walter et al., 2014) or oxygen-producing photosynthetic bacteria (Klein and Beukes, 1989). The organic carbon isotope data from the spheroidal fossiliferous Girar-Baraitha BIF support the major role of anoxygenic photosynthesizers rather than the role of oxygen-producing cyanobacteria (Fig. 9).

The consistently low total organic carbon (TOC) observed in Archean banded iron formations (BIFs) likely reflects both environmental constraints and post-depositional processes. During the Archean, biological productivity was limited, particularly due to the absence or early stages of oxygenic photosynthesis, resulting in reduced organic carbon input to marine sediments. Simultaneously, the ferruginous nature of Archean oceans, with abundant dissolved Fe^{2+}–favored the rapid formation of iron oxides, which may have facilitated the oxidation and breakdown of organic material. Furthermore, the scarcity of clay and detrital minerals in many BIFs would have limited the physical protection of organic matter, making it more susceptible to degradation. Over time, thermal alteration and redox-driven diagenesis or metamorphism may have further diminished TOC by converting residual organic compounds into graphite or gaseous forms. These combined factors explain the characteristically low organic carbon content in Archean BIFs.

6. Conclusions

This study confirms the presence of *Huroniospora*-like microfossils in the Mesoarchean Girar Banded Iron Formation (BIF) of the Bundelkhand craton, representing the oldest convincing record of microfossils from BIF to date. Morphological and isotopic evidence suggests that while these microfossils bear a resemblance to *Huroniospora*, they cannot be described by one distinct metabolic pathway. Instead, the δ^{13}C-org values point to affinities with anoxygenic photosynthesisers, methanogenic archaea, methanotrophic bacteria, and, to a limited extent, cyanobacteria. The study proposes two primary mechanisms for Fe^{2+} oxidation: biotic oxidation mediated by anaerobic phototrophs (photoferrotrophs) and abiotic oxidation via dissolved O_2 under suboxic conditions, with the former being dominant, particularly around or below the shallow chemocline. Geochemical proxies, specifically Sm/Yb versus Eu/Sm ratios, indicate a significant influence of hydrothermal fluids mixed with seawater at ratios ranging from 1:1000 to 1:100. The shallow marine setting likely experienced mildly elevated levels of dissolved oxygen, reaching suboxic conditions conducive to limited abiotic oxidation of Fe^{2+}. Collectively, these observations provide potential evidence for microbial mediation in Precambrian iron deposition and support the view that oxygenic photosynthesis was not the principal mechanism driving early BIF formation, underscoring the importance of anaerobic microbial processes in Earth's early iron cycle.

CRediT authorship contribution statement

Arif H. Ansari: Writing – review & editing, Writing – original draft, Visualization, Validation, Supervision, Resources, Project administration, Methodology, Investigation, Funding acquisition, Formal analysis, Data curation, Conceptualization. **Yogmaya Shukla:** Writing – original draft, Visualization, Validation, Investigation, Formal analysis. **Gaurav K. Singh:** Writing – original draft, Visualization, Investigation, Formal analysis, Data curation. **Archana Sonker:** Investigation, Formal analysis, Data curation. **Mohammad Arif Ansari:** Methodology, Investigation, Formal analysis, Data curation. **Arunaditya Das:** Writing – review & editing, Visualization, Validation, Methodology, Formal analysis.

Declaration of competing interest

The authors declare that they have no known competing financial interests or personal relationships that could have appeared to influence the work reported in this paper.

Acknowledgment

We sincerely thank the Director of BSIP for continuous support and encouragement throughout this project. We also extend our gratitude to Srinivas Bikkina and Anupam Sharma for facilitating SAIF instruments., We acknowledge Ishwar Rahi, and Subodh Kumar for their technical support in the sample analysis. This research is part of BSIP Project 1. The BSIP contribution number for this manuscript is BSIP/RDCC/Publication No. 100/2024-2025.

Data availability

No data was used for the research described in the article.

References

Agnihotri, R., Gahlaud, S., Patel, N., Sharma, R., Kumar, P., Chopra, S., 2020. Radiocarbon measurements using new automated graphite preparation laboratory coupled with stable isotope mass-spectrometry at Birbal Sahni Institute of Palaeosciences, Lucknow (India). J. Environ. Radioact. 213, 106156.

Alexander, B.W., Bau, M., Andersson, P., Dulski, P., 2008. Continentally-derived solutes in shallow Archean seawater: rare earth element and Nd isotope evidence in iron formation from the 2.9 Ga Pongola Supergroup, South Africa. Geochem. Cosmochim. Acta 72, 378–394.

Alibo, D.S., Nozaki, Y., 1999. Rare earth elements in seawater: particle association, shale-normalization, and Ce oxidation. Geochem. Cosmochim. Acta 63, 363–372.

Anbar, A.D., Duan, Y., Lyons, T.W., Arnold, G.L., Kendall, B., Creaser, R.A., Kaufman, A. J., Gordon, G.W., Scott, C., Garvin, J., 2007. A whiff of oxygen before the great oxidation event? Science 317, 1903–1906.

Ansari, A., Pandey, S., Ahmad, S., Sharma, M., Govil, P., Chaddha, A.S., Sharma, A., 2023. High primary productivity in an Ediacaran shallow marine basin influenced by strong seasonal to perennial upwelling. Geol. Mag. 160, 1607–1623.

Ansari, A.H., Ahmad, S., Govil, P., Agrawal, S., Mathews, R.P., 2020. Mo-Ni and organic carbon isotope signatures of the mid-late Mesoproterozoic oxygenation. J. Asian Earth Sci. 191, 104201.

Awramik, S.M., Barghoorn, E.S., 1977. The gunflint microbiota. Precambr. Res. 5, 121–142.

Barghoorn, E.S., Tyler, S.A., 1965. Microorganisms from the Gunflint Chert: these structurally preserved Precambrian fossils from Ontario are the most ancient organisms known. Science 147, 563–575.

Barrett, T.J., Jarvis, I., Longstaffe, F.J., Farquhar, R., 1988. Geochemical aspects of hydrothermal sediments in the eastern Pacific Ocean; an update. Can. Mineral. 26, 841–858.

Bau, M., Dulski, P., 1999. Comparing yttrium and rare earths in hydrothermal fluids from the Mid-Atlantic Ridge: implications for Y and REE behaviour during near-vent mixing and for the Y/Ho ratio of Proterozoic seawater. Chem. Geol. 155, 77–90.

Bau, M., Möller, P., 1993. Rare earth element systematics of the chemically precipitated component in Early Precambrian iron formations and the evolution of the terrestrial atmosphere-hydrosphere-lithosphere system. Geochem. Cosmochim. Acta 57, 2239–2249.

Bekker, A., Eriksson, K.A., 2003. A Paleoproterozoic drowned carbonate platform on the southeastern margin of the Wyoming Craton: a record of the Kenorland breakup. Precambr. Res. 120, 327–364.

Bekker, A., Slack, J.F., Planavsky, N., Krapez, B., Hofmann, A., Konhauser, K.O., Rouxel, O.J., 2010. Iron formation: the sedimentary product of a complex interplay among mantle, tectonic, oceanic, and biospheric processes. Econ. Geol. 105, 467–508.

Bengtson, S., Sallstedt, T., Belivanova, V., Whitehouse, M., 2017. Three-dimensional preservation of cellular and subcellular structures suggests 1.6 billion-year-old crown-group red algae. PLoS Biol. 15, e2000735.

Bolhar, R., Kamber, B.S., Moorbath, S., Fedo, C.M., Whitehouse, M.J., 2004. Characterisation of early Archaean chemical sediments by trace element signatures. Earth Planet Sci. Lett. 222, 43–60.

Braterman, P.S., Cairns-Smith, A.G., Sloper, R.W., 1983. Photo-oxidation of hydrated Fe2+—significance for banded iron formations. Nature 303, 163–164.

Broderick, T.M., 1919. Detail stratigraphy of the Biwabik iron-bearing formation, east Mesabi District, Minnesota. Econ. Geol. 14, 441–451.

Butterfield, N.J., 2000. Bangiomorpha pubescens n. gen., n. sp.: implications for the evolution of sex, multicellularity, and the Mesoproterozoic/Neoproterozoic radiation of eukaryotes. Paleobiology 26, 386–404.

Campbell, K.A., Lynne, B.Y., Handley, K.M., Jordan, S., Farmer, J.D., Guido, D.M., Foucher, F., Turner, S., Perry, R.S., 2015. Tracing biosignature preservation of geothermally silicified microbial textures into the geological record. Astrobiology 15, 858–882.

Cloud Jr., P.E., 1965. Significance of the Gunflint (Precambrian) Microflora: photosynthetic oxygen may have had important local effects before becoming a major atmospheric gas. Science 148, 27–35.

Cloud Jr., P.E., Hagen, H., 1965. Electron microscopy of the Gunflint microflora: preliminary results. Proc. Natl. Acad. Sci. 54, 1–8.
Cloud Jr., P.E., Licari, G.R., 1968. Microbiotas of the banded iron formations. Proc. Natl. Acad. Sci. 61, 779–786.
Colleps, C., McKenzie, N., Sharma, M., Liu, H., Gibson, T., Chen, W., Stockli, D., 2021. Zircon and apatite U-Pb age constraints from the Bundelkhand craton and Proterozoic strata of central India: insights into craton stabilization and subsequent basin evolution. Precambr. Res. 362, 106286.
Courty, P.-E., Walder, F., Boller, T., Ineichen, K., Wiemken, A., Rousteau, A., Selosse, M.-A., 2011. Carbon and nitrogen metabolism in mycorrhizal networks and mycoheterotrophic plants of tropical forests: a stable isotope analysis. Plant Physiol. 156, 952–961.
Danielson, A., Möller, P., Dulski, P., 1992. The europium anomalies in banded iron formations and the thermal history of the oceanic crust. Chem. Geol. 97, 89–100.
Derry, L.A., Jacobsen, S.B., 1990. The chemical evolution of Precambrian seawater: evidence from REEs in banded iron formations. Geochem. Cosmochim. Acta 54, 2965–2977.
Dymek, R.F., Klein, C., 1988. Chemistry, petrology and origin of banded iron-formation lithologies from the 3800 Ma Isua supracrustal belt, West Greenland. Precambr. Res. 39, 247–302.
Farquhar, J., Wing, B.A., 2003. Multiple sulfur isotopes and the evolution of the atmosphere. Earth Planet Sci. Lett. 213, 1–13.
Grey, K., 1999. A Modified Palynological Preparation Technique for the Extraction of Large Neoproterozoic Acanthomorph Acritarchs and Other Acid-Soluble Microfossils.
Gruner, J.W., 1922. Organic matter and the origin of the Biwabik iron-bearing formation of the Mesabi range. Econ. Geol. 17, 407–460.
Gruner, J.W., 1924. Bulletin No. 19. Contributions to the Geology of the Mesabi Range with Special Reference to the Magnetites of the Iron-Bearing Formation West of Mesaba.
Halevy, I., Bachan, A., 2017. The geologic history of seawater pH. Science 355, 1069–1071.
Harder, E.C., 1919. Iron-depositing Bacteria and Their Geologic Relations. US Government Printing Office.
Hiloidari, S., Satyanarayanan, M., Singh, S.P., Bhutani, R., Subramanyam, K., Sarma, D. S., 2021. Evidence for mesoarchean subduction in southern Bundelkhand craton, India: geochemical fingerprints from metavolcanics of Kurrat-Girar-Badwar greenstone belt. Geochemistry 81, 125787.
Hobbie, E.A., Boyce, C.K., 2010. Carbon sources for the Palaeozoic giant fungus Prototaxites inferred from modern analogues. Proc. Biol. Sci. 277, 2149–2156.
House, C.H., Schopf, J.W., McKeegan, K.D., Coath, C.D., Harrison, T.M., Stetter, K.O., 2000. Carbon isotopic composition of individual Precambrian microfossils. Geology 28, 707–710.
Jacobsen, S.B., Pimentel-Klose, M.R., 1988. A Nd isotopic study of the Hamersley and Michipicoten banded iron formations: the source of REE and Fe in Archean oceans. Earth Planet Sci. Lett. 87, 29–44.
Javaux, E.J., Knoll, A.H., Walter, M.R., 2004. TEM evidence for eukaryotic diversity in mid-Proterozoic oceans. Geobiology 2, 121–132.
Joshi, M.P., Samanta, A., Tripathy, G.R., Rajamani, S., 2017. Formation and stability of prebiotically relevant vesicular systems in terrestrial geothermal environments. Life (Basel) 7.
Kappler, A., Straub, K.L., 2005. Geomicrobiological cycling of iron. Rev. Mineral. Geochem. 59, 85–108.
Kaur, P., Zeh, A., Chaudhri, N., 2014. Characterisation and U–Pb–Hf isotope record of the 3.55 Ga felsic crust from the Bundelkhand Craton, northern India. Precambr. Res. 255, 236–244.
Kaur, P., Zeh, A., Chaudhri, N., Eliyas, N., 2016. Unravelling the record of Archaean crustal evolution of the Bundelkhand Craton, northern India using U–Pb zircon–monazite ages, Lu–Hf isotope systematics, and whole-rock geochemistry of granitoids. Precambr. Res. 281, 384–413.
Kendall, B., Reinhard, C.T., Lyons, T.W., Kaufman, A.J., Poulton, S.W., Anbar, A.D., 2010. Pervasive oxygenation along late Archaean ocean margins. Nat. Geosci. 3, 647–652.
Klein, C., 2005. Some Precambrian banded iron-formations (BIFs) from around the world: their age, geologic setting, mineralogy, metamorphism, geochemistry, and origins. Am. Mineral. 90, 1473–1499.
Klein, C., Beukes, N.J., 1989. Geochemistry and sedimentology of a facies transition from limestone to iron-formation deposition in the early Proterozoic Transvaal Supergroup, South Africa. Econ. Geol. 84, 1733–1774.
Knoll, A.H., Simonson, B., 1981. Early proterozoic microfossils and penecontemporaneous quartz cementation in the sokoman Iron Formation, Canada. Science 211, 478–480.
Knoll, A.H., Strother, P.K., Rossi, S., 1988. Distribution and diagenesis of microfossils from the lower Proterozoic Duck Creek Dolomite, Western Australia. Precambr. Res. 38, 257–279.
Konhauser, K.O., Amskold, L., Lalonde, S.V., Posth, N.R., Kappler, A., Anbar, A., 2007. Decoupling photochemical Fe (II) oxidation from shallow-water BIF deposition. Earth Planet Sci. Lett. 258, 87–100.
Konhauser, K.O., Hamade, T., Raiswell, R., Morris, R.C., Ferris, F.G., Southam, G., Canfield, D.E., 2002. Could bacteria have formed the Precambrian banded iron formations? Geology 30, 1079–1082.
Konhauser, K.O., Planavsky, N., Hardisty, D., Robbins, L., Warchola, T., Haugaard, R., Lalonde, S., Partin, C., Oonk, P., Tsikos, H., 2017. Iron formations: a global record of Neoarchaean to Palaeoproterozoic environmental history. Earth Sci. Rev. 172, 140–177.
Kremer, B., Kaźmierczak, J., 2017. Cellularly preserved microbial fossils from~ 3.4 Ga deposits of South Africa: a testimony of early appearance of oxygenic life? Precambr. Res. 295, 117–129.
Lanier, W.P., 1989. Interstitial and peloid microfossils from the 2.0 Ga Gunflint Formation: implications for the paleoecology of the Gunflint stromatolites. Precambr. Res. 45, 291–318.
Leith, C.K., 1903. The Mesabi Iron-Bearing District of Minnesota. US Government Printing Office.
Lepot, K., 2020. Signatures of early microbial life from the Archean (4 to 2.5 Ga) eon. Earth Sci. Rev. 209, 103296.
Lepot, K., Addad, A., Knoll, A.H., Wang, J., Troadec, D., Béché, A., Javaux, E.J., 2017. Iron minerals within specific microfossil morphospecies of the 1.88 Ga Gunflint Formation. Nat. Commun. 8, 14890.
Li, Y.-L., Konhauser, K.O., Kappler, A., Hao, X.-L., 2013. Experimental low-grade alteration of biogenic magnetite indicates microbial involvement in generation of banded iron formations. Earth Planet Sci. Lett. 361, 229–237.
Luskin, C., Wilson, A., Gold, D., Hofmann, A., 2019. The pongola supergroup: mesoarchaean deposition following kaapvaal craton stabilization. The archaean geology of the kaapvaal craton. South. Afr. 225–254.
Lyons, T.W., Reinhard, C.T., Planavsky, N.J., 2014. The rise of oxygen in Earth's early ocean and atmosphere. Nature 506, 307–315.
Malviya, V.P., Arima, M., Pati, J.K., Kaneko, Y., 2006. Petrology and geochemistry of metamorphosed basaltic pillow lava and basaltic komatiite in the Mauranipur area: subduction related volcanism in the Archean Bundelkhand craton, Central India. J. Mineral. Petrol. Sci. 101, 199–217.
Malviya, V.P., Arima, M., Verma, S.K., K Pati, J., Shareef, M., L Dora, M., K Singh, V., Prakash, S., Shukla, M., 2022. Petrology and geochemistry of the Palaeo-Mesoarchean Banded Iron formations (BIFs) from the central Bundelkhand greenstone belts, Bundelkhand craton, India: source characteristics and depositional environment. Geol. J. 57, 3292–3312.
Mayor, J.R., Schuur, E.A., Henkel, T.W., 2009. Elucidating the nutritional dynamics of fungi using stable isotopes. Ecol. Lett. 12, 171–183.
Michard, A., Albarède, F., 1986. The REE content of some hydrothermal fluids. Chem. Geol. 55, 51–60.
Mondal, M., Goswami, J., Deomurari, M., Sharma, K., 2002. Ion microprobe 207Pb/206Pb ages of zircons from the Bundelkhand massif, northern India: implications for crustal evolution of the Bundelkhand–Aravalli protocontinent. Precambr. Res. 117, 85–100.
Mondal, M.E.A., Ahmad, T., 2001. Bundelkhand mafic dykes, central Indian shield: implications for the role of sediment subduction in Proterozoic crustal evolution. Isl. Arc 10, 51–67.
Moore, E., 1918. The iron-formation on Belcher Islands, Hudson Bay, with special reference to its origin and its associated algal limestones. J. Geol. 26, 412–438.
Morris, R., 1993. Genetic modelling for banded iron-formation of the Hamersley group, Pilbara craton, Western Australia. Precambr. Res. 60, 243–286.
Morris, R., Horwitz, R., 1983. The origin of the iron-formation-rich Hamersley Group of Western Australia—deposition on a platform. Precambr. Res. 21, 273–297.
Mukhopadhyay, J., 2020. Archean banded iron formations of India. Earth Sci. Rev. 201, 102927.
Nke, A.Y., Tsikos, H., Mason, P.R., Mhlanga, X., Tostevin, R., 2024. A seawater origin for greenalite in iron formation. Earth Planet Sci. Lett. 643, 118917.
Nozaki, Y., Zhang, J., Amakawa, H., 1997. The fractionation between Y and Ho in the marine environment. Earth Planet Sci. Lett. 148, 329–340.
O'Neil, J., 2023. Nuvvuagittuq Greenstone Belt, Encyclopedia of Astrobiology. Springer, pp. 2131–2135.
Ogura-Tsujita, Y., Yukawa, T., 2008. Epipactis helleborine shows strong mycorrhizal preference towards ectomycorrhizal fungi with contrasting geographic distributions in Japan. Mycorrhiza 18, 331–338.
Ostrander, C.M., Heard, A.W., Shu, Y., Bekker, A., Poulton, S.W., Olesen, K.P., Nielsen, S. G., 2024. Onset of coupled atmosphere–ocean oxygenation 2.3 billion years ago. Nature 1–5.
Ostrander, C.M., Johnson, A.C., Anbar, A.D., 2021. Earth's first redox revolution. Annu. Rev. Earth Planet Sci. 49, 337–366.
Ostrander, C.M., Nielsen, S.G., Owens, J.D., Kendall, B., Gordon, G.W., Romaniello, S.J., Anbar, A.D., 2019. Fully oxygenated water columns over continental shelves before the Great Oxidation Event. Nat. Geosci. 12, 186–191.
Pati, J., Patel, S., Pruseth, K., Malviya, V., Arima, M., Raju, S., Pati, P., Prakash, K., 2007. Geology and geochemistry of giant quartz veins from the Bundelkhand Craton, central India and their implications. J. Earth Syst. Sci. 116, 497–510.
Pecoits, E., Smith, M., Catling, D., Philippot, P., Kappler, A., Konhauser, K., 2015. Atmospheric hydrogen peroxide and Eoarchean iron formations. Geobiology 13, 1–14.
Peng, Y., Kusky, T., Wang, L., Luan, Z., Wang, C., Liu, X., Zhong, Y., Evans, N.J., 2022. Passive margins in accreting Archaean archipelagos signal continental stability promoting early atmospheric oxygen rise. Nat. Commun. 13, 7821.
Planavsky, N., Bekker, A., Rouxel, O.J., Kamber, B., Hofmann, A., Knudsen, A., Lyons, T. W., 2010. Rare earth element and yttrium compositions of Archean and Paleoproterozoic Fe formations revisited: new perspectives on the significance and mechanisms of deposition. Geochem. Cosmochim. Acta 74, 6387–6405.
Planavsky, N.J., Reinhard, C.T., Wang, X., Thomson, D., McGoldrick, P., Rainbird, R.H., Johnson, T., Fischer, W.W., Lyons, T.W., 2014. Low Mid-Proterozoic atmospheric oxygen levels and the delayed rise of animals. Science 346, 635–638.
Posth, N.R., Hegler, F., Konhauser, K.O., Kappler, A., 2008. Alternating Si and Fe deposition caused by temperature fluctuations in Precambrian oceans. Nat. Geosci. 1, 703–708.

Posth, N.R., Konhauser, K.O., Kappler, A., 2013. Microbiological processes in banded iron formation deposition. Sedimentology 60, 1733–1754.
Pradhan, V.R., Meert, J.G., Pandit, M.K., Kamenov, G., Mondal, M.E.A., 2012. Paleomagnetic and geochronological studies of the mafic dyke swarms of Bundelkhand craton, central India: implications for the tectonic evolution and paleogeographic reconstructions. Precambr. Res. 198, 51–76.
Ramiz, M.M., Mondal, M., 2017. Petrogenesis of Mafic Magmatic Enclaves of the Bundelkhand Granitoids Near Orchha, Central Indian Shield: Evidence for Rapid Crystallization, 449. Geological Society, London, Special Publications, pp. 159–173.
Rasmussen, B., Buick, R., 1999. Redox state of the Archean atmosphere: evidence from detrital heavy minerals in ca. 3250–2750 Ma sandstones from the Pilbara Craton, Australia. Geology 27, 115–118.
Rasmussen, B., Muhling, J., Krapež, B., 2021. Greenalite and its role in the genesis of early Precambrian iron formations–A review. Earth Sci. Rev. 217, 103613.
Robbins, L.J., Funk, S.P., Flynn, S.L., Warchola, T.J., Li, Z., Lalonde, S.V., Rostron, B.J., Smith, A.J., Beukes, N.J., de Kock, M.O., 2019. Hydrogeological constraints on the formation of Palaeoproterozoic banded iron formations. Nat. Geosci. 12, 558–563.
Roday, P.P., Diwan, P., Singh, S., 1995. A kinematic model of emplacement of quartz reefs and subsequent deformation patterns in the central Indian Bundelkhand batholith. Proc. Indian Acad. Sci. Earth Planet Sci. 104, 465–488.
Roday, P.P., Maheshwari, G., Vaghmarey, N.H., 1990. R i-μ i/μ m-C i dependent oblateness of deformed pebbles in the Baraitha conglomerate, Central India and tectonic implications. Proc. Indian Acad. Sci. Earth Planet Sci. 99, 321–338.
Saha, L., Pant, N.C., Pati, J.K., Upadhyay, D., Berndt, J., Bhattacharya, A., Satynarayanan, M., 2011. Neoarchean high-pressure margarite-phengitic muscovite-chlorite corona mantled corundum in quartz-free high-Mg, Al phlogopite-chlorite schists from the Bundelkhand craton, north central India. Contrib. Miner. Petrol. 161, 511–530.
Sánchez-Baracaldo, P., Raven, J.A., Pisani, D., Knoll, A.H., 2017. Early photosynthetic eukaryotes inhabited low-salinity habitats. Proc. Natl. Acad. Sci. 114, E7737–E7745.
Schidlowski, M., 2001. Carbon isotopes as biogeochemical recorders of life over 3.8 Ga of Earth history: evolution of a concept. Precambr. Res. 106, 117–134.
Sergeev, V., Seong-Joo, L., 2004. New Data on Silicified Microfossils from the Satka Formation of the Lower Riphean Stratotype, the Urals.
Shapiro, R., Konhauser, K., 2015. Hematite-coated microfossils: primary ecological fingerprint or taphonomic oddity of the Paleoproterozoic? Geobiology 13, 209–224.
Sibelev, O., Slabunov, A., Mishra, S., Singh, V., 2021a. Metamorphism of the Central Bundelkhand greenstone complex, Indian shield: mineral compositions, paragenesises, and P–T path. Petrology 29, 404–438.
Sibelev, O.S., Slabunov, A.I., Singh, V.K., Mishra, S., 2021b. Metamorphism of the central Bundelkhand greenstone complex of the Bundelkhand craton, Indian shield and its geodynamic setting. Geological. Geo-Environ. Process. Earth 143–154.
Simonson, B.M., Chan, M., Archer, A., 2003. Origin and Evolution of Large Precambrian Iron Formations. Special Papers-Geological Society of America, pp. 231–244.
Singh, V.K., Nesterova, N., Slabunov, A., Singh, M., 2019. Tectonic divisions of the Bundelkhand Craton Indian Shield: on the basis of geological, geophysical and Sm-Nd systematic of granitoids data. National Seminar on Geological Aspects of Northwest Indian Shield. on March, pp. 15–16.
Singh, V.K., Slabunov, A., 2015. The Central Bundelkhand Archaean greenstone complex, Bundelkhand craton, central India: geology, composition, and geochronology of supracrustal rocks. Int. Geol. Rev. 57, 1349–1364.
Singh, V.K., Slabunov, A., 2016. Two types of Archaean supracrustal belts in the Bundelkhand Craton, India: geology, geochemistry, age and implication for craton crustal evolution. J. Geol. Soc. India 88, 539–548.
Singh, V.K., Slabunov, A., Nesterova, N., Singh, M., Bhatt, S., 2021. Tectonostratigraphic terranes of the Bundelkhand craton (Indian shield). Geol. Geo-Environ. process. Earth 155–164.
Slabunov, A., Egorova, S., Singh, V.K., Svetov, S., Kumar, S., 2018. Archean mafic-ultramafic Ikauna layered intrusion, Bundelkhand craton, India: petrography and geochemistry. Arch. Anthropol Open Acc. 3, 49–55.
Slabunov, A., Joshi, K.B., Singh, S.K., Rai, V.K., 2024. Depositional age and formation conditions of Archean banded iron formations, Bundelkhand Craton, Central India: geochemistry, neodymium isotopes and U-Pb zircon geochronology. Precambr. Res. 401, 107254.
Slabunov, A., Singh, V.K., Joshi, K.B., Li, X., 2017. Paleoarchean zircons from quartzite of south Bundelkhand supracrustal complex: origin and implications for crustal evolution in Bundelkhand craton, Central India. Curr. Sci. 794–801.
Slabunov, A.I., Singh, V.K., 2021. Crustal evolution of Bundelkhand Craton in Archean and comparison with other Indian cratons. In: *Geological and geo-environmental processes on Earth*. Springer Singapore, Singapore, pp. 39–48.
Slabunov, A.I., Singh, V.K., 2022. Giant quartz veins of the Bundelkhand craton, Indian shield: new geological data and U-Th-Pb age. Minerals 12, 168.
Slabunov, A., Singh, V.K., 2019. Meso–Neoarchaean crustal evolution of the Bundelkhand Craton, Indian Shield: new data from greenstone belts. Int. Geol. Rev. 61, 1409–1428.
Slack, J., Grenne, T., Bekker, A., Rouxel, O., Lindberg, P., 2007. Suboxic deep seawater in the late Paleoproterozoic: evidence from hematitic chert and iron formation related to seafloor-hydrothermal sulfide deposits, central Arizona, USA. Earth Planet Sci. Lett. 255, 243–256.
Slack, J.F., Grenne, T., Bekker, A., 2009. Seafloor-hydrothermal Si-Fe-Mn exhalites in the Pecos greenstone belt, New Mexico, and the redox state of ca. 1720 Ma deep seawater. Geosphere 5, 302–314.
Slotznick, S.P., Johnson, J.E., Rasmussen, B., Raub, T.D., Webb, S.M., Zi, J.-W., Kirschvink, J.L., Fischer, W.W., 2023. Response to comment on "Reexamination of 2.5-Ga 'whiff' of oxygen interval points to anoxic ocean before GOE". Sci. Adv. 9, eadg1530.
Smith, A.J., Beukes, N.J., Gutzmer, J., 2013. The composition and depositional environments of Mesoarchean iron formations of the west rand group of the witwatersrand supergroup, South Africa. Econ. Geol. 108, 111–134.
Sreenivas, B., Murakami, T., 2005. Emerging views on the evolution of atmospheric oxygen during the Precambrian. J. Mineral. Petrol. Sci. 100, 184–201.
Strother, P.K., Tobin, K., 1987. Observations on the genus Huroniospora Barghoorn: implications for paleoecology of the gunflint microbiota. Precambr. Res. 36, 323–333.
Suetsugu, K., Matsubayashi, J., Tayasu, I., 2020. Some mycoheterotrophic orchids depend on carbon from dead wood: novel evidence from a radiocarbon approach. New Phytol. 227, 1519–1529.
Sugitani, K., 2019. Cellular microfossils and possible microfossils in the paleo-and mesoarchean. Astrobiology: Orig. Life Search Extraterr. Intell. 229–259.
Taylor, S., McLennan, S., 1986. The Chemical Composition of the Archaean Crust, 24. Geological Society, London, Special Publications, pp. 173–178.
Thompson, K.J., Kenward, P.A., Bauer, K.W., Warchola, T., Gauger, T., Martinez, R., Simister, R.L., Michiels, C.C., Llirós, M., Reinhard, C.T., 2019. Photoferrotrophy, deposition of banded iron formations, and methane production in Archean oceans. Sci. Adv. 5, eaav2869.
Viehmann, S., Bau, M., Hoffmann, J.E., Münker, C., 2015. Geochemistry of the Krivoy Rog Banded Iron Formation, Ukraine, and the impact of peak episodes of increased global magmatic activity on the trace element composition of Precambrian seawater. Precambr. Res. 270, 165–180.
Viswanathiah, M., Venkatachalapathy, V., 1980. Microbiota from the Bababudan iron formation, Karnataka. J. Geol. Soc. India 21, 16–20.
Walter, M.R., Goode, A., Hall, W., 1976. Microfossils from a newly discovered Precambrian stromatolitic iron formation in Western Australia. Nature 261, 221–223.
Walter, X.A., Picazo, A., Miracle, M.R., Vicente, E., Camacho, A., Aragno, M., Zopfi, J., 2014. Phototrophic Fe (II)-oxidation in the chemocline of a ferruginous meromictic lake. Front. Microbiol. 5, 713.
Wang, C., Dong, Z., Robbins, L., Zhang, B., Peng, Z., Tong, X., Zhang, L., Konhauser, K., 2024a. A craton-wide geochemical survey of late Archean banded iron formations in China. Earth Planet Sci. Lett. 642, 118879.
Wang, C., Xie, S., Zhang, X., Tong, X., Bai, Y., Peng, Z., Dong, Z., Zhang, L., Wan, B., 2024b. Deciphering the source of banded iron formations in the North China Craton. Precambr. Res. 402, 107298.
Warke, M.R., Strauss, H., Schröder, S., 2020. Positive cerium anomalies imply pre-GOE redox stratification and manganese oxidation in Paleoproterozoic shallow marine environments. Precambr. Res. 344, 105767.
Williford, K.H., Ushikubo, T., Schopf, J.W., Lepot, K., Kitajima, K., Valley, J.W., 2013. Preservation and detection of microstructural and taxonomic correlations in the carbon isotopic compositions of individual Precambrian microfossils. Geochem. Cosmochim. Acta 104, 165–182.
Yun, Z., 1984. A Gunflint type of microfossil assemblage from early Proterozoic stromatolitic cherts in China. Nature 309, 547–549.